



Published in final edited form as:

Exp Eye Res. 2020 May ; 194: 107998. doi:10.1016/j.exer.2020.107998.

Axonal debris accumulates in corneal epithelial cells after intraepithelial corneal nerves are damaged: A focused Ion Beam Scanning Electron Microscopy (FIB-SEM) study

Paola Parlanti^{a,1}, Sonali Pal-Ghosh^b, Alexa Williams^b, Gauri Tadvalkar^b, Anastas Popratiloff^{a,b}, Mary Ann Stepp^{b,c,*}

^aGW Nanofabrication and Imaging Center, The George Washington School of Medicine and Health Sciences, Washington DC, 20052, USA

^bDepartment of Anatomy and Cell Biology, The George Washington School of Medicine and Health Sciences, Washington DC, 20052, USA

^cDepartment of Ophthalmology, The George Washington School of Medicine and Health Sciences, Washington DC, 20052, USA

Abstract

The intraepithelial corneal nerves (ICNs) that innervate the corneal epithelium are maintained through interactions with corneal epithelial cells and the extracellular matrix they produce. One to several axons bundle together within the basal cell layer and extend parallel to the ocular surface or branch and extend apically. Here we use 3-dimensional (3D) ultrastructural reconstructions of control and trephine injured mouse corneal epithelium and stroma produced using Focused Ion Beam Scanning Electron Microscope (FIB-SEM) to determine whether corneal epithelial or immune cells resident in the epithelium remove axonal debris and degrade it in their lysosomes after trephine injury to the cornea. We demonstrate that axonal fragments are internalized in the corneal epithelium and accumulate within electron dense structures consistent with lysosomes 3 h after trephine injury in both epithelial and immune cells located among the basal cells of the trephine injured cornea. Confocal imaging showed fewer CD45⁺ immune cells within the corneal epithelium after trephine injury compared to controls. The resolution obtained using FIB-SEM also allowed us to show that the presence of sensory axons at the basal aspect of the epithelial basal cells close to the anterior aspect of the epithelial basement membrane (EBM) is associated with a focal reduction in EBM thickness. In addition, we show using FIB-SEM and confocal imaging that superficial trephine injuries that do not penetrate the stroma, damage the integrity of anterior stromal nerves. These studies are the first to look at the mouse cornea following nerve injury using FIB-SEM.

This is an open access article under the CC BY-NC-ND license (<http://creativecommons.org/licenses/by-nc-nd/4.0/>).

*Corresponding author. Department of Anatomy and Cell Biology, GWSMHS, 2300 I St. NW Ross Hall Rm 231, Washington DC, 20052, USA. mastepp@gwu.edu (M.A. Stepp).

[†]Current address: Child Health Institute of New Jersey, Department of Neuroscience and Cell Biology, Robert Wood Johnson Medical School, Rutgers, NJ 08901.

Appendix A. Supplementary data

Supplementary data to this article can be found online at <https://doi.org/10.1016/j.exer.2020.107998>.

Keywords

Cornea; Corneal nerves; FIB-SEM; Trephine injury; Mouse

1. Introduction

The unmyelinated sensory axons present in the human cornea epithelium, travel millimeters within the basal layer of the epithelium without the aid of *bona fide* glial cells. After penetrating the basement membrane and entering the epithelium through the corneal stroma, these nerves course parallel to the basement membrane while branching and extending apically towards the apical squames. The corneal epithelial cells wrap around the axons and protect them from mechanical injury caused by blinking and eye rubbing and function as surrogate glial cells (Stepp et al., 2017). The nerves have abundant mitochondria and, because the cornea is transparent, mitochondria are exposed to UV light. Fragments of axons including their damaged mitochondria are shed between or within corneal epithelial cells. We propose that these shed fragments are phagocytosed by the corneal epithelial cells and accumulate in lysosomes several hours after axon shedding is induced by crush wounds using a dull trephine (Stepp et al., 2017). The ability of corneal epithelial cells to phagocytose axon debris shares features with the events that take place in the retina where RPE cells phagocytose shed rod and cone outer segments to maintain optimal photoreceptor function (Kevany and Palczewski, 2010).

ICNs are the peripheral processes of trigeminal ganglion C (80%) and A- δ (20%) fibers; they conduct temperature and non-discriminative pain stimuli to the ophthalmic branch of the trigeminal ganglion (Lwigale, 2001; Nakamura et al., 2007; Shaheen et al., 2014). C-fibers are unmyelinated and of low conductance velocity (Acosta et al., 2001). In pioneering work conducted in the 1980's by Rosza and Beuerman among others (Beuerman and Rozsa, 1984; Rozsa and Beuerman, 1982; Rozsa et al., 1983), the sensory nerves in the rabbit cornea were described using colloidal gold and/or silver stains. Vertebrate corneal nerve studies were also performed in the cat (Marfurt, 1981) and rat (Marfurt and Del Toro, 1987) using retrograde labeling with horse radish peroxidase. The nerves were referred to as subbasal nerves (SBNs) organized into a subbasal nerve plexus (SNP) with nerve terminals (NTs) that extended apically. The phrase "subbasal" suggests that the nerves are below the corneal epithelial basal cells. Since these cells adhere to their basement membrane via hemidesmosomes and form adhesion complexes that penetrate the anterior stroma (Stepp et al., 1990), having a high density of nerves beneath the basement membrane would impact the adhesion of the epithelium to the stroma.

In the late 1990's, Linda Muller began working with transmission electron microscopy (TEM) to assess the corneal nerves (Muller et al., 1996, 1997). In 2003, a landmark paper was published (Muller et al., 2003) using transmission electron microscopy (TEM) that showed that while SBNs associate with the basal aspect of the corneal epithelial cells, rather than being located under the epithelium, the nerves are actually within the epithelium covered by the cells' basal and basolateral membranes. There is a renewed interest in these nerves as they are deemed to be responsible for corneal pain and discomfort in dry eye

disease and can be studied in patients using in vivo confocal imaging (Cruzat et al., 2017; Hamrah et al., 2017). We suggested in 2017 that the nerves be referred to as intraepithelial corneal nerves (ICNs) (Stepp et al., 2017). Here we refer to the axons previously called the subbasal nerves as Intraepithelial Corneal Basal Nerves (ICBNs); the nerve terminals we refer to as the Intraepithelial Corneal Nerve Terminals (ICNTs). When the term ICN is used, it refers to both ICBNs and ICNTs (Stepp et al., 2020).

All cells are capable of phagocytosing debris. Corneal epithelial cells were shown to phagocytose particulate matter by Niederkorn and colleagues (Niederkorn et al., 1989) and bacteria by Fleiszig and colleagues (Fleiszig et al., 1995). Their ability to function as phagocytes is regulated by cell surface proteins including $\alpha v \beta 5$ integrin (Buommino et al., 2014) and syndecan-1 (Pal-Ghosh et al., 2017). We set out here to confirm that the corneal epithelial cells are capable of functioning as phagocytes to clear axonal debris after nerve injury. To achieve this goal, we used a trephine injury mouse cornea wound model (Pajooheh-Ganji et al., 2015) along with high resolution backscatter scanning electron microscopy imaging combined with serial focused ion beam milling of block faces (FIB-SEM). The approach produces a series of electron microscopy resolution images that are registered as 3-dimensional (3D) sets and enables us to structure the 3D data by manually segmenting the ICNs to follow their interaction with epithelial and immune cells. The images from control corneal epithelial cells show the close association between the ICBNs and the epithelial basement membrane (EBM). Confocal imaging was performed to determine the numbers and morphologies of immune cells within the epithelium and to assess the status of the corneal stromal nerves after trephine injury. These studies illustrate the utility of FIB-SEM for ultrastructural analysis of the intraepithelial corneal nerves.

2. Methods

2.1. Trephine injury

All studies performed were approved by The George Washington University Institutional Animal Care and Use Committee guidelines and in compliance with the ARVO Statement for the Use of Animals in Ophthalmic and Vision Research. For these studies, 7- to 8-week male BALB/cN mice were used. Mice were anesthetized with ketamine/xylazine and a topical anesthetic applied to their ocular surface as described previously (Pal-Ghosh et al., 2017). For trephine wounds, a 1.5-mm dulled trephine was applied gently to the ocular surface and rotated once (180°) leaving a visible depression on the ocular surface that defines the proximal (corneal periphery) and distal (towards corneal center) sites. After injury, topical erythromycin ophthalmic ointment was applied to prevent infection and keep the ocular surface moist until anesthesia wears off and blinking resumes. Unless otherwise indicated, mice were allowed to recover for 3 h after trephine injury followed by euthanization using CO_2 and tissue collected and fixed for confocal imaging or for FIB-SEM studies as described below. Control mice were also included in these studies. A minimum of 3 corneas were assessed for each time point of FIB-SEM, confocal imaging, and stromal nerve studies. All confocal microscopy and FIB-SEM was carried out at the GW Nanofabrication and Imaging Center at The George Washington University.

2.2. FIB-SEM tissue processing

For FIB-SEM, corneas were dissected from the retina and lens and fixed in 4% paraformaldehyde and 0.5% glutaraldehyde for 2 h at room temperature. After a brief rinse in sodium cacodylate buffer, corneas were cut in half, and flattened on a silicon support followed by postfixation overnight in 2.5% glutaraldehyde and 2% paraformaldehyde. After aldehyde fixation, corneas were processed according to a protocol adapted from those previously described (Deerinck, 2010; Kheirkhah et al., 2015; Parlanti et al., 2017, 2019). All incubations were performed at room temperature. Briefly, tissues were incubated for 1 h in a solution containing 2% osmium tetroxide and 1.5% potassium ferricyanide in 0.1 M sodium cacodylate buffer, then for 20 min in 1% thiocarbohydrazide aqueous solution, followed by 30 min treatment with aqueous 2% osmium tetroxide. Samples were incubated overnight in 1% uranyl acetate aqueous solution, and finally in lead aspartate. These additional steps of heavy metal staining enhanced the contrast of the tissue and improved the signal for the backscattered electron imaging. After the *en bloc* staining, samples were dehydrated in a graded series of ethanol, flat-embedded in epoxy resin and polymerized at 60 °C for 48 h.

Embedded corneas were then mounted vertically on SEM aluminum stubs (Ted Pella Inc., Redding, CA, USA) with the central region facing up, and the sides covered with silver conductive epoxy (Ted Pella Inc., Redding, CA, USA), which was cured at 60 °C for 12 h. Each sample was sectioned, using a UC7 ultramicrotome (Leica, Wetzlar, Germany), into 500 nm thin cross sections using a glass knife and visualized using an optical microscope (Olympus). Once the section (and then the sample's flattened block face) showed the epithelium, the epithelial basement membrane (EBM), and the anterior stroma, we further cut 120 nm thin sections using a diamond knife (Diatome, Switzerland), which were placed on a silicon wafer (Ted Pella Inc., Redding, CA, USA), attached on a SEM stub through carbon conductive tab (Ted Pella Inc., Redding, CA, USA). The ultramicrotome sectioning represents a crucial step in FIB-SEM analysis and allowed the imaging of corneas with high-resolution SEM to locate the regions of interest in the tissue where the FIB-SEM would be performed on the block face. In addition, sectioning using a diamond knife polishes the block face. After sectioning, corneal blocks mounted on SEM stubs were sputter coated with 0.5 nm iridium to increase the sample conductivity.

2.3. FIB-SEM tomography

2.3.1. Regions of interest identification—The strategic selection of a meaningful region of interest within a cross sectioned cornea was critical to drive the FIB-SEM analysis. For each cornea, an ultrathin section immediately before the final polished corneal block face was collected for high resolution backscatter SEM (Helios 660 NanoLab Dual Beam FIB-SEM, Thermo Fisher Scientific Electron Microscopy Solutions, Hillsboro, OR, USA). This ultrathin section was imaged with 2 kV, 400 pA landing current using insertable solid state concentric back scattered (CBS) detector in immersion mode. This setup supports high resolution imaging using low acceleration voltages. The Helios NanoLab 660 also runs Maps 3.8 software (Thermo Fisher Scientific Electron Microscopy Solutions, Hillsboro, OR, USA), which enables collection of layered low resolution and linked high resolution image sets to be spatially associated, as well as navigation through the sample using low

resolution imaging. We captured lower and higher resolution layers of the 120 nm sections, to identify the areas of interest for serial block face imaging. Using Maps software, the two-dimensional large area composite images were aligned with the block face. Before the preparation step for serial block-face imaging, another round of electron beam scanning was performed on the sample block face using 5 kV landing voltage, which led to increased electron interaction volume ensuring detection of signal from below the iridium protection layer. The later step is necessary to confirm the location of the selected area of interest.

A more detailed discussion of the instrument capabilities, detectors, and software is provided in Supplemental Methods.

2.3.2. Sample preparation for serial block face imaging—Once the area of interest was located, we could perform the FIB-SEM serial block face imaging. The sample was first positioned at 52°, the area subjected to serial ion (gallium) milling was covered with 2 µm platinum (Pt), and the cross section exposed by creating a trench approximately 25 µm deep and 30 µm wide. Additionally, two fiducial markers were created for the automatic alignment of ion and electron images. Further details of sample preparation are provided in Supplementary Materials.

2.3.3. Serial block face milling imaging—The instrument is equipped with the Auto Slice and View 4.0 software (ASV, Thermo Fisher Scientific, Waltham, MA, USA) which enables execution of repeated sequential operations leading to generation of sequential electron images taken at consistent intervals (40 nm). The stage was set to 52° tilt for ion milling, at an eucentric height of about 4 mm; the accelerating voltage for milling was 30 kV with landing beam current of 790 pA. Once a section was milled, the stage was moved to 45° while the working distance was set to 2.5 mm. A shorter working distance was necessary to increase the incidence of elastically scattered electrons entry into the column and reaching the Through Lens Detector (TLD). For electron imaging 2 kV acceleration voltage and 400 pA landing current routinely provide excellent signal to noise and low white noise with a resolution of 3072×2048 pixels and a dwell time of 10 µsec. After image acquisition using the ASV 4.0 software, the stage was automatically moved to the milling position. The number of cycles were determined by the preset size of the y-axis, which determines the final z-size of the volume.

The milled “slice” thickness (40 nm), the working distance, and all ion beam parameters for milling and electron beam for imaging were kept consistent. Relative magnification varied slightly between experiments, depending on the features of interest, so the pixel size varied accordingly between 5 and 17 nm. In this work we compare volumes at the same magnification. The number of sequential slices producing the volumes used for analyses varied between ~150 (6 µm total z-axis analyzed) and ~350 sections (14 µm in z-axis).

2.3.4. Volume registration, image segmentation and analysis—The re-alignment of the field of view to fiducial markers was essential to correct for the slight beam shifts in x and y axis and compensate for sample instability between milling and imaging. However, the series of electron images were still not compliant with robust 3D-registration. We took advantage of various software packages during the different steps of

image analysis. Image alignment was performed with Dragonfly (Objects Research Systems Inc., Montreal, QC, Canada), an open source tool with high capabilities for image analysis. Amira (Thermo Fisher Scientific, Waltham, MA, USA) was used for volume cropping, filtering and brightness and contrast optimization. Arivis Vision 4D (Arivis AG, Munich, Germany) was used for manual segmentation, and to generate 3D movies and images of the segmented volumes. Finally, ImageJ and Photoshop (Adobe Inc., San Jose, CA, USA) were used respectively for volume inspection and image generation for this manuscript.

2.4. Whole mount immunostaining

Eyes were fixed immediately after euthanization in a paraformaldehyde-containing fixative (1x PBS, 1% formaldehyde, 2-mM MgCl₂, 5-mM EGTA, 0.02% NP-40) for 1 h and 15 min at 4 °C, followed by two washes for 10 min each in PBS containing 0.02% NP40 at room temperature. Tissues were then placed in 4:1 methanol:dimethyl sulfoxide (DMSO) for 2 h at -20 °C and then stored in 100% methanol at -20 °C until used for whole-mount staining studies. The back of the eye was cut and the retina, lens, and iris removed before staining. Tissues were transferred to a graded Methanol-TritonX-100 series (75%, 50%, and 25% methanol:TritonX-100 for 15, 15, and 10 min, respectively). All incubations were performed with gentle shaking and at room temperature, unless otherwise specified. The eyes were washed twice in PBS, for 30 min each, followed by incubation with blocking buffer for 2 h. Blocking buffer was made as follows: to 100 mL 1x PBS, 1 g of BSA was added, the mixture was stirred for 10 min, 1 mL of horse serum was added, and the mixture was stirred for an additional minute.

The corneas were incubated overnight with primary antibody diluted in blocking buffer at 4 °C. The following antibodies were used: neuron specific β III tubulin (TUJ1; #801201; Biolegend, San Diego, CA, USA), and CD45 (30-F11; #103101; Biolegend, San Diego, CA, USA). Appropriate secondary DyLite 488 and 594 antibodies from Jackson Immunobiologicals (West Grove, PA, USA) were used for immunolabeling fluorescence detection. The next day, the tissues were washed five times with PBS and 0.02% Tween 20 (PBST) for 1 h each, blocked for 2 h, and then incubated with secondary antibody diluted in blocking buffer overnight at 4 °C. The following day, corneas were washed three times with PBST for 1 h each, followed by nuclear staining with 4,6-diamidino-2- phenylindole (DAPI) for 5 min, and washed with distilled water. To achieve the best flattening, the corneas were placed epithelial side-up with mounting media (#17984-25, Fluoromount G; Electron Microscopy Sciences; Hatfield, PA, USA) and coverslipped.

2.5. Confocal microscopy

For images in Fig. 8, a confocal laser-scanning microscope (Zeiss 710; Carl Zeiss, Inc., Oberkochen, Germany) was used to image the localization of Alexa Fluor 488 (CD45) (argon laser; 488-nm laser line excitation; 495/562 emission slit opening; Jackson Immunobiologicals) and Alexa Fluor 594 (β III tubulin) (561 diode laser; 594-nm laser line excitation; 601/649 emission slit opening; Jackson Immunobiologicals). Optical sections (0.5 μ m) were acquired sequentially with a 63x/1.40 NA objective lens. Three-dimensional (3D) images were rotated to generate cross section views using Volocity software (Version 6.3; PerkinElmer, New York, NY, USA). High-resolution images were presented either

as cross sections projected through the length of the acquired image (135 μm), or as cross-sections projected through 0.5 μm of tissue.

En face confocal images for nerves (βIII tubulin) in Figs. 1 and 5 (25 \times magnification) were acquired using the Zeiss Cell Observer Z1 spinning disk confocal microscope (Carl Zeiss, Inc., Thornwood, NY, USA), equipped with ASI MS-2000 (Applied Scientific Instrumentation, Eugene, OR, USA) scanning stage with z-galvo motor, and Yokogawa CSU-X1 spinning disk. A multi-immersion 25x/0.8 objective lens, LCI Plan-Neofluor, was used for imaging, with oil immersion. Evolve Delta (Photometrics, Tucson, AZ, USA) 512 \times 512 EMCCD camera was used as detector (80-msec exposure time). A diode laser emitting at 568 nm was used for excitation (54% power). Zen Blue software (Carl Zeiss, Inc.) was used to acquire the images, fuse the adjacent tiles, and produce maximum intensity projections. The adjacent image tiles were captured with overlap to ensure proper tiling.

3. Results

3.1. FIB-SEM visualizes intraepithelial corneal basal nerves (ICBNs) extending parallel to the corneal epithelial basement membrane (EBM) in healthy mouse corneas

The architecture of the ICNs in the unwounded mouse cornea is visualized schematically and in *en face* confocal imaging using an antibody against βIII tubulin in Fig. 1. Axons enter the epithelium from the stroma by penetrating the EBM. The majority of these penetration sites are at the corneal periphery (Stepp et al., 2020). *En face* projection images focus attention on the ICBN component of the ICNs. ICBNs terminate near the corneal center at the vortex. To understand ICN morphology within epithelial cells proximal and distal to the trephine injury site, it was necessary to start our FIB-SEM studies assessing the ICBNs in unwounded corneas. To optimize qualitative and quantitative outcomes and visualization of the stromal and intraepithelial corneal nerves in the mouse by serial block face imaging, numerous different fixation and tissue preparation methods were tested. These different approaches were needed to enhance our ability to visualize the axons within the epithelium. Digging trenches deep enough to penetrate the anterior stroma and visualize the corneal epithelial basal cells as sections are cut serially over time was accomplished after several test runs. The procedures used to fix the tissue and stain them are described in detail in the methods section.

A movie showing the sections acquired in control tissues is provided in supplemental data (Supplemental Movie 1). In Fig. 2A, the block face of a control cornea is shown with the area indicated where milling takes place. Two images from control corneas showing the interface between epithelium and stroma are presented in Fig. 2B and C with both images presented in duplicate. The bottom images are presented with labels and corneal epithelial, axonal, and Schwann cell membranes delineated using green, orange, and yellow lines respectively whereas the images above remain without added markings. Numerous membrane systems are present within corneal epithelial cells. The EBM separates the epithelium and stroma. Corneal epithelial cell nuclei contain numerous nuclear invaginations. Earlier studies using serial FIB-SEM have revealed nuclear invaginations in numerous different cell types (Jorgens et al., 2017; Shimojima et al., 2017) and authors have suggested that they play a role in mediating gene expression (Uhler and Shivashankar,

2017). Condensed chromatin in nuclei is not observed. Attempts to increase the sensitivity of the detector to enhance the signal from chromatin and hemidesmosomes at the EBM resulted in saturation of the signal from the epithelial cytoplasm making it impossible to resolve ICNs, mitochondria, and putative primary lysosomes within the epithelium.

Supplementary video related to this article can be found at <https://doi.org/10.1016/j.exer.2020.107998>

Primary lysosomes, derived from endosomes, convert into secondary lysosomes once they fuse with endosomes containing organelles to be degraded or phagocytosed debris (Luzio et al., 2014; Saftig and Klumperman, 2009). In the control cornea, using FIB-SEM, it was not possible to distinguish primary lysosomes from endosomes or small mitochondria imaged in cross section; we do label two putative primary lysosomes in Panel C. Axons (orange highlight) are observed at the far right in B and at the center in C within epithelial cells above the EBM. In the stroma, in Panel B, a Schwann cell (yellow highlight) is seen wrapped around several axons of a stromal nerve; in Panel C, stromal cells are seen.

ICBN and stromal nerve axons contain numerous mitochondria. Mitochondria vary in diameter between 0.1 and 1 μM and in length from 3 to 10 μM (Flatters, 2015; Hamid et al., 2014; Villegas et al., 2014). In Panel B, several epithelial cell mitochondria (eM) are observed in longitudinal section and, in panel C, one is seen in cross section. Axonal mitochondria (aM) are also seen in Panels B and C. In panel B, mitochondria are seen within ICBN and stromal nerve axons in cross section; inner mitochondrial membranes (cristae) are observed. Mitochondria are also seen within axons of an ICBN in longitudinal section in Panel C.

Electron dense granules of various sizes are present within the epithelial cytoplasm. These granules have morphologies similar to glycogen granules (de Bruijn, 1973) that have been reported previously in TEM studies of corneal epithelial cells (Kuwabara et al., 1976; Muller et al., 1996). Besides glycogen granules and mitochondria, the control corneal epithelial cytoplasm contains few electron dense structures. Well-ordered collagen bundles are present in the stroma. The stromal nerve shown in Panel B consists of a non-myelinating Schwann cell wrapped around several axons imaged in cross section that contain numerous mitochondria. Both Schwann cell and axonal membranes are visible. The deeper stroma shown in Panel C shows stromal cells sandwiched between collagen lamellae. Keratocytes, unlike Schwann cells, have abundant endoplasmic reticulum in their cytoplasm.

3.2. ICBNs adjacent to the EBM reduce basement membrane thickness

The images 1–5 shown in Fig. 3 are sequential images that focus attention on the relationship between ICBNs and the EBM. The EBM thickness was measured from left to right along the EBM of each image using Image J at 20 sites per image; a total of 100 measurements were obtained. Beneath each image, a graph showing EBM thickness as a function of the distance along the EBM from left to right is presented. At sites where the EBM appears to disappear entirely, values of 0 were assigned. We highlight three regions: EBM sites that have no ICBNs associated with them (axon-free, A-F, blue lines), EBM sites where axons are present and viewed in cross section as determined by the circular

mitochondria they contain (CS, green lines), and EBM sites where axons are viewed in longitudinal section as determined by the elongated rod-like shapes of the axons and their mitochondria (LS, maroon lines). The mean EBM thickness was determined for each of these three regions and is presented graphically in Fig. 3. Mean EBM thickness was the same for areas lacking axons and where ICBNs were imaged in cross section but was significantly lower by ANOVA for sites where ICBNs were imaged in longitudinal section. Chi square analysis comparing differences in the numbers of EBM thickness values that were 0 between the three groups yields a Chi square value of 12.79 which is also significant ($p = 0.0017$).

Sequential 2-dimensional (2D) images were used to perform segmentation and generate 3D renderings to demonstrate the paths taken by individual ICBNs as shown in Supplemental Movies 2 and 3; Supplemental Movie 4 shows an ICNT. The three images shown in Fig. 4A were obtained from Supplemental Movie 2 and demonstrate the paths taken by ICBNs in the control corneal epithelium. The image in the middle shows, in cross section, 5 individual axons each segmented in a different color. Segmentation of these axons shows that they extend above the basement membrane as seen in the images above and below. While 4 of the 5 axons segmented traveled along similar paths, one of them (aqua) enters the epithelium at a different site, merges with the other axons temporarily, and then heads off in another direction. The image shown in Fig. 4B was taken from Supplemental Movie 3. In this movie, the EBM is segmented (purple); rather than assigning each axon a different color, all axons are colored yellow. The volume has been rotated to focus attention on the area where the electron density that typically defines the EBM thins and disappears. The image shown in Fig. 4C was obtained from Supplemental Movie 4 and shows an ICNT moving between epithelial cells away from the basement membrane towards the corneal apical surface. The ICNT contains a single axon. While more difficult to image, we are still able to follow ICNTs using FIB-SEM.

Supplementary video related to this article can be found at <https://doi.org/10.1016/j.exer.2020.107998>

3.3. By 3 h after corneal injury, ICN loss is observed in the corneal center within the area defined by the trephine

Fig. 5A shows schematic representations and confocal images of whole flat mounted control corneas stained to reveal ICNs using an antibody against β III tubulin to reflect our current understanding of ICN morphology and the changes seen in response to 1.5 mm trephine injury. Fig. 5A also shows confocal images of whole flat mounted corneas showing ICNs 3 h and 24 h after trephine injury. Distal to the injury site (cornea center-within the area defined by the trephine), ICBNs and ICNTs degenerate because their connection to their nerve cell body in the trigeminal ganglion has been severed. Degenerating axons are often referred to as beading. Once cell membrane integrity is lost, axons fragment. The beads consist of axonal debris surrounding axonal mitochondria. Proximal to the injury site (corneal periphery-outside the area defined by the trephine), ICNs remain attached to their nerve cell body; after injury-triggered retraction, they begin to reinnervate the central cornea. By 3 h, axon loss distal to the wound site begins and by 24 h, there is significant loss of ICNs in

the corneal center distal to the injury site; in previous studies, we showed that 50% of the axons are lost after 1.5 mm trephine injury (Pajooohesh-Ganji et al., 2015; Pal-Ghosh et al., 2017). While ICNs that entered the epithelium outside the trephine site are severed, those that enter the epithelium from the stroma within the trephine site are retained along with the vortex. Higher magnification images obtained at 24 h after injury show fewer axons at the center and, at the periphery, axons have begun to reinnervate the distal site. Damage to corneal epithelial cells is restricted to the site where the trephine blade crushes the epithelial cells (Pajooohesh-Ganji et al., 2015)

3.4. Axonal debris can be seen in corneal epithelial basal cells and immune cells proximal and distal to the wound crush site

In Fig. 6A, a block face of a trephine injured cornea 3 h after injury is shown. The area where the trephine blade crushed the corneal epithelium is indicated by the arrows and the sites where milling took place are indicated by the asterisks; we first look proximal to the injury site where severed nerves remain attached to stromal nerves and trigeminal ganglion cell bodies. Previous studies have shown that proximal axons retract during the first 6 h after trephine injury (Stepp et al., 2017). A movie showing the FIB-SEM data acquired from a trephine injured cornea is shown in Supplemental Movie 5. In Fig. 6B1–5 and 6C1–5, serial images are presented from two different corneas imaged using FIB-SEM of the proximal region. Higher magnification images are presented below in Fig. 6Bi–v and Fig. 6Ci–v. In Fig. 6B1/Bi, a bundle of 3–4 axons is shown. The axons appear swollen (engorged) and three of the four mitochondria present are electron dense; the axon on the right contains microtubules but no mitochondria. Panels 6B2–5 and, at higher magnification in 6B*ii*–v, show electron dense material within structures consistent with their identification as secondary lysosomes (Hayashi et al., 2009; Roggia and Ueta, 2015) The lysosome shown in Fig. 6Bv appears to show an axon fragment at an earlier stage of degradation whereas those in Fig. 6Bii and iv show more advanced stages of degradation of their contents. Glycogen granules are reduced or absent at proximal sites after trephine injury.

Supplementary video related to this article can be found at <https://doi.org/10.1016/j.exer.2020.107998>

The images of the proximal corneal epithelium shown in Fig. 6C1–5 also show the basal epithelial cell: stromal interface; however, in this series of images an immune cell comes into view in Fig. 6C4 and is shown clearly in Fig. 6C5. The cytoplasm of the immune cell differs from that of the surrounding epithelial cells; the basal surface of the immune cells does not interact directly with the EBM but overlays a thin area of corneal epithelial cytoplasm and cell membrane. Fig. 6C1–2 and 6Ci–ii show ICBNs containing mitochondria; while the mitochondria in 6Ci appears healthy, the axons in 6Cii contain two extremely electron dense mitochondria indicating that they are degenerating. 6C3–5 and 6Ciii–v also show electron dense material within structures consistent with lysosomes. 6Cv shows the interaction between the immune cells and the corneal epithelial cell; both cell types contain electron dense material within lysosomes. Supplemental Movie 6 was obtained from the proximal site and shows segmentation of an ICBN within the epithelium and 3 lysosomes. Two lysosomes are within the epithelial cells and one is within an immune cell. The data

presented in Fig. 6 show that severing ICBNs induces accumulation of electron dense material within lysosomes in uninjured corneal epithelial cells located proximal to the injury site.

More axonal debris has to be cleared at distal sites where severed axons completely degenerate compared to proximal sites. In Fig. 7A, the block face of a trephine injured cornea obtained 3 h after injury is presented to show the area where the trephine blade crushed the corneal epithelium as indicated by the arrows. The sites where milling took place are indicated by the asterisks; here we focus on sites distal to the injury site. The images shown in Fig. 7B1–3 and 7C1–3 were taken from two different corneas imaged using FIB-SEM serial sectioning of the distal region; areas of interest are shown at higher magnification in Fig. 7Bi-iii and 7Ci-iii. Fig. 7B2–7B3 and 7Bii-iii show an immune cell present within the epithelium. Electron dense material within lysosomes is shown in Fig. 7B1 and 7Bi. Along with the epithelial cells, the immune cell seen in Fig. 7B3 and 7Biii is actively phagocytosing and degrading axonal debris as evidenced by the presence of electron dense material in its cytoplasm within structures consistent with their identification as lysosomes. The immune cell in 7Biii also contains an axon that appears engorged and swollen. Its degradation by the immune cell appears to just be beginning.

The images shown in Fig. 7C1–3 also show an epithelial cell in the distal region with several large electron dense structures consistent with their identification as secondary lysosomes. The lysosome shown in Fig. 7C1 and 7Ci appears to be actively degrading a mitochondrion as well as axonal debris. Fig. 7C2/7C3 and 7Cii/7Ciii also highlight electron dense material within epithelial cells. While numerous ICBNs are present at the basal aspect of the epithelial cells shown in Fig. 7C, healthy mitochondria containing cristae are absent or missing in all three images shown. As observed for proximal sites, glycogen granules are also reduced or absent at distal sites after trephine injury.

3.5. CD45⁺ immune cells decrease in number in 3 h trephine injured corneas compared to controls

Immune cells were not observed in the control corneas we assessed by FIB-SEM; yet, we know that CD45⁺ cells are present within the control corneal epithelium (Pal-Ghosh et al., 2014; Saban, 2014). The intraepithelial immune cells present in the corneal epithelium are MHC + dendritic cells that play roles in ocular inflammation and protection from microorganisms. *En face* confocal images projected through 30 μm (60 layers of 0.5 μm each) of control and the distal sites of trephine injured corneas are presented projected from beneath the epithelial basement membrane towards the anterior aspect of the cornea are shown in Fig. 8A. Elongated CD45⁺ dendritic cells are present within the epithelial basal cell layer that are closely associated with ICBNs. We next quantified the numbers of CD45⁺ dendritic cells at the periphery of control and proximal sites of trephine injured corneas 3 h after injury. There are significantly fewer CD45⁺ cells in the periphery of the trephine injured cornea compared to controls. A reduction in the numbers of immune cells within the epithelial compartment has been shown previously by us (Stepp et al., 2018) and others (Jiao et al., 2019). The control images on the left are obtained at the corneal periphery; on the right, round CD45⁺ cells are seen at the corneal center. Gao and colleagues (Gao et

al., 2016) have also reported two distinct shapes of intraepithelial immune cells associated with corneal nerves. 3 h after trephine injury, the morphologies of the immune cells at the periphery are similar to those seen at the control periphery. However, at the corneal center after trephine injury, we observe both round and elongated immune cells.

We next obtained 3D confocal images from trephine wounded corneas at proximal and distal sites using Volocity as described in the methods section. We present in Fig. 8B *en face* and cross-sectional views showing CD45⁺ immune cells and axons. Immune cells are retained within the basal compartment of the epithelium after trephine injury; while apically oriented projections can be seen at proximal locations, no projections could be seen in images acquired from distal sites. While immune cells aid in removing axonal debris generated by severing the ICBNs within basal epithelial cells, they are not present and, therefore, do not play a role in clearing debris from severed ICNTs that degenerate within suprabasal, wing, and apical squames after trephine injury.

3.6. Trephine injury doesn't penetrate the stroma yet induces stromal axon loss

To confirm that the trephine injury site did not penetrate the stroma, 3 h after wounding, we obtained images directly at the injury site. Data are shown in Fig. 9A. Note the lack of nuclei and disordered cytoplasm seen in the epithelial cells indicating that the epithelial cells have died traumatically via a mechanism referred to as accidental cell death (ACD) (Galluzzi et al., 2018). The epithelial basement membrane is intact. The basal aspect of the epithelial basal cell region where ICBNs are most abundant in control corneas is electron lucent; axonal membranes and mitochondria are not detected. While the stroma and stromal keratocytes appear healthy, stromal nerves imaged in longitudinal section show electron lucent sites suggesting pathology. These images confirm the crushing of epithelial cells and ICBNs at the trephine site by 3 h. We next imaged stromal cells in the proximal and distal sites 3 h after trephine injury; we present a representative image from a proximal site. Compared to the control cornea (Fig. 2), stromal cells appear dysmorphic and swollen (Fig. 9A).

We next asked whether the stromal nerves were also reduced after trephine injury. To investigate this possibility, we trephine injured the mouse cornea and sacrificed mice at 3, 6, and 18 h after injury and compared arborization of the stromal nerves to that seen in uninjured controls. Representative images and their quantification are presented in Fig. 9B. Data show that stromal nerve arborization is significantly reduced after trephine injury and remains low for at least 18 h.

4. Discussion

By combining SEM imaging techniques with serial sectioning, FIB-SEM is a powerful technique that can be used to determine ultrastructure within the tissues and show how different elements within cells interact with one another. The mammalian cornea is an ideal tissue to use this approach on. It is accessible, organized into distinct layers, and has been well studied by transmission electron microscopy. Further, the nerves in the corneal epithelium play important roles in vision by controlling blinking and protecting the cornea from injuries.

In vivo confocal imaging is being used on patients to reveal the ICNs and the causes of ocular pain and discomfort secondary to trauma and disease (Cruzat et al., 2017; De Silva et al., 2017; Dieckmann et al., 2017; Hamrah et al., 2017; Patel and McGhee, 2005; Tervo et al., 2016; Villani et al., 2014).

4.1. Corneal epithelial and immune cells mediate clearance of axonal debris from ICBNs after trephine injury

Since ICNs are exposed directly to UV light; their mitochondria are expected to get damaged frequently. Rather than transport damaged mitochondria, proteins, and lipids to lysosomes in the nerve cell body in the trigeminal ganglion to be degraded, it would take less time and energy if, after injury, axon fragments and their mitochondria were shed and phagocytosed by the corneal epithelial cells whose cell membranes surround them. The ability of corneal epithelial cells to function as non-professional phagocytes, has been appreciated for many years (Fleiszig et al., 1995; Niederkorn et al., 1989). In zebrafish, epithelial cells and not immune cells have been shown to function as phagocytes to remove axon debris in response to injury (Rasmussen et al., 2015).

Here we show that corneal epithelial basal cells function as phagocytes to ingest axonal debris generated by trephine injury and degrade it in lysosomes located in the epithelial basal cell layer at both distal and proximal locations. We also show that immune cells with morphologies consistent with their identification as dendritic cells are present (Gao et al., 2016; Hamrah and Dana, 2007; Kheirikhah et al., 2015; Seyed-Razavi et al., 2019) and are also active in the removal of axonal debris within the basal cell layer at both proximal and distal locations. In the peripheral control cornea, confocal imaging showed that immune cells can associate with numerous ICBNs simultaneously. In the central control cornea, immune cells are round and small (10–15 μm); at the corneal periphery and, in the proximal and distal trephine injured corneas, immune cells extend for distances of over 100 μm . The fact that immune cells are elongated makes it easier to capture them in the FIB-SEM images at the proximal and distal locations in the trephine injured corneas. All of the serial sectioning in control corneas involved the central cornea; FIB-SEM did not detect any immune cells in controls. While we used a general immune cell marker (CD45) to visualize the immune cells by confocal imaging, the immune cells present in the corneal epithelial basal cell layer have been shown by others to be CD11C + MHC Class II + dendritic cells (Gao et al., 2016; Jiao et al., 2019). Immune cells have been reported to play roles in neuroinflammation (Belmonte et al., 1997; Jiao et al., 2019; Launay et al., 2016; McKay et al., 2019).

Data presented show that immune cells in the basal cell layer also accumulate debris in lysosomes after trephine injury and help clear debris from severed ICBNs. ICNTs are also severed after trephine injury and their mitochondria and axonal debris also are cleared after injury. No immune cells are present suprabasally to assist the corneal epithelial cells in clearing the ICNT debris. Thus, corneal epithelial cells exclusively remove ICNT debris suprabasally.

Damaged or severed axons can lead to the death of neuron cell bodies. An example of this phenomenon is seen in glaucoma at the optic nerve where elevated intraocular pressure

crushes nerve fibers from the retinal ganglion cells as they exit the globe leading to death of retinal ganglion cells and vision loss (Almasieh et al., 2012; Kerrigan-Baumrind et al., 2000). Injury to the ICNs, whether induced by debridement, chemical injury, or dry eye, will lead to propagation of signals from injured axons through the stromal nerves to the nerve cell body in the trigeminal ganglion (Fakih et al., 2019; Martinez and Belmonte, 1996; Valyi-Nagy et al., 1991). We show here that trephine injury is accompanied by a significant decrease in stromal nerve arborization. Because ICNs completely recover 3 days after trephine injury (Pal-Ghosh et al., 2017) it is unlikely that there is a loss of trigeminal ganglion nuclei in this model. The exact mechanism leading to fewer stromal nerves after trephine injury is not known. It could be the result of die-back of proximal ICBNs and the stromal nerves they branch from or to stromal swelling after injury. We do not yet know whether stromal nerve arborization recovers as quickly as ICN density after trephine injury.

4.2. Axonal mitochondria and their involvement in sensory nerve neuropathy

The abundance of axonal mitochondria in ICBNs and their electron density allowed their degradation within lysosomes to become a focus of our study. Degeneration of axonal mitochondria has been proposed to lead to axonal degeneration in a number of neurodegenerative pathologies (Court and Coleman, 2012) including the small fiber neuropathy in skin associated with diabetes (Brines et al., 2018).

A recent paper by Villegas and colleagues (Villegas et al., 2014) shows the role played by calcium release from axonal endoplasmic reticulum (ER) after axons are severed. The presence of ER, mRNA, and protein synthesis in peripheral axons began to be appreciated only recently (Gumy et al., 2010); the implications for understanding neurodegeneration are beginning to be studied. After axons are severed, calcium release from axonal ER leads to axonal mitochondrial swelling, rupturing, and shrinking which increases their electron density (Schmidt et al., 2008). Ishibashi and colleagues (Ishibashi et al., 2016) show that the increased bead sizes seen in vivo in confocal images of ICBNs in corneas of patients with type 2 diabetes were associated with slower conduction velocities of the ulnar and sural nerve peripheral nerves. The enlarged bead sizes seen in diabetic corneal nerves have been attributed to mitochondrial swelling (Hamid et al., 2014). These studies and others are leading to the use of in vivo confocal imaging of the cornea to understand therapeutic responses of patients, including those with diabetes, to various treatments for small fiber neuropathy (Brines et al., 2018).

4.3. FIB-SEM shows glycogen stores are depleted in response to trephine injury in corneal epithelial cells proximal and distal to the trephine injury site

Using FIB-SEM, we can see that control corneal epithelial basal cells contain abundant glycogen in their cytoplasm. Corneal epithelial cells have been reported to have high intracellular stores of glycogen (Kuwabara et al., 1976) that decrease in response to corneal epithelial debridement injury (Ogita, 1978) as glycogen is converted to glucose which is used for energy via glycolysis. The images and movies we have obtained provide support for those observations made using TEM and extend them to trephine injuries. After trephine injury, the electron dense granules present in the epithelial cell cytoplasm disappear at distal and proximal locations in basal cells adjacent to the trephine injury sites. The cells at these

sites have not been injured directly. This would provide the cells with energy needed to phagocytose the shed axonal debris.

4.4. FIB-SEM shows the close association between corneal epithelial cells, ICBNs, and ICNTs

We do not describe the morphology of the stromal nerve epithelial penetration sites. Our movies were acquired to focus on the epithelium. Courson and colleagues (Courson et al., 2019) have assessed sites where stromal nerves penetrate the EBM in adult mice using serial block face scanning electron microscopy (SBF-SEM). SBF-SEM allows larger fields of view (Peddie and Collinson, 2014); while that advantage comes at the cost of lower resolution, both SBF-SEM and FIB-SEM provide exceptional advantages compared to traditional TEM.

The non-myelinating Schwann cells that surround the stromal nerves secrete a basement membrane (basal lamina) that surrounds individual and clusters of axons. Schwann cells remain in the stroma when stromal nerve axons enter the epithelium and become ICBNs. Their basal lamina is replaced by ECM synthesized by corneal epithelial basal cells. We recently reported that, as stromal nerves penetrate the EBM, they lose expression of syndecan-3 (*sd3*), a heparan sulfate proteoglycan expressed by Schwann cells (Asundi et al., 2003; Goutebroze et al., 2003); *sd3* on ICBNs is replaced by LN332 which is produced by corneal epithelial cells (Stepp et al., 2020).

While not assessed in the mammalian cornea, nociceptive sensory neurons have been shown to induce the epithelial cells they interact with to secrete a basal lamina during development and homeostasis (Jiang et al., 2019; Tenenbaum et al., 2017); this process is referred to as ensheathment and has been shown to regulate axonal branching and nociceptive sensitivity. A recent study in *Drosophila* and zebrafish revealed the mechanisms used by axons to induce epithelial cells to wrap them in ECM proteins (Jiang et al., 2019). The molecules and machinery used to form and stabilize the sheaths are similar in both fish and flies.

4.5. EBM thinning and its potential role in maintaining ICBNs at the basal aspect of the epithelial basal cells

Corneal epithelial cells adhere to the EBM and stroma via hemi-desmosome-based adhesion complexes (Stepp et al., 1990). These include type IV, XV, and XVIII collagens, laminins, perlecan and nidogens (Randles et al., 2017). The FIB-SEM data presented in control corneas suggests that ICBNs are in close proximity to an EBM that is thinner than the EBM at sites lacking ICBNs. When ICBNs are imaged in longitudinal section, extensive regions of close interaction between ICBN and the EBM can be visualized. These sites of close contact were 4–6 μm long. When imaged in cross section, sites of close contact are limited. Significant EBM thinning was only observed when ICBNs are viewed in longitudinal but not cross section. This is likely due to thinning being restricted to the overall diameter of the ICBN that overlays the EBM. ICBNs may compete for EBM proteins secreted basally or basolaterally by corneal epithelial basal cells.

The FIB-SEM data presented here suggests potential involvement of the ICBNs in pathologies associated with EBM. Recurrent corneal erosion syndrome is often characterized as secondary to dysfunctional corneal epithelial cells (Lin et al., 2019; Miller

et al., 2019; Watson and Leung, 2018). Erosions develop secondary to superficial trauma or in patients with epithelial basement membrane degeneration. When corneal innervation is eliminated surgically, recurrent erosions develop within days (Ferrari et al., 2011). While the mechanism underlying erosion formation in this model is thought to be loss of stem cell identity, EBM integrity has not been assessed. Reduced secretion of ECM by corneal epithelial cells due to pathology, trauma, or aging could contribute to erosions by thinning the EBM and lead to ocular pain. These are important areas that need additional research.

How the ICBNs are maintained within the basal aspect of the corneal epithelial basal cells is not known. Like all stratified squamous epithelia, corneal epithelial basal cells differentiate, detach from the EBM, and enter the suprabasal cell layer. Over time the cells are desquamated. EBM thinning adjacent to sites where ICBNs associate with the EBM offers possible mechanisms for further studies to investigate how the ICBNs are maintained within the basal aspect of the cell layer.

Axon targeting has been extensively studied in development and after injury in vitro and in vivo (Berzat and Hall, 2010; Myers et al., 2011; O'Donnell et al., 2009) and a large number of secreted molecules have been identified that regulate axon guidance (Shaheen et al., 2014). If stromal cells (Schwann cells, keratocytes, and/or immune cells) release factors that attract the ICBNs during homeostasis, it could explain why the nerves are maintained within the basal aspect of the basal cells near sites where the EBM is thin. We performed RNAseq on RNA isolated from control and debridement wounded mouse corneal stromas (Stepp et al., 2017). Studying the RNAseq data set reveals expression of RNAs encoding several genes that regulate axonal targeting expressed by corneal stromal cells including several semaphorins, *Sprr1a*, *Netrin1*, *Unc5b*, *Efna4*, and *Efna5* in RNA in the corneal stromas. Secretion of these molecules by stromal cells and their diffusion into the epithelial compartment through the EBM could maintain ICBNs at the basal aspect of the basal epithelial cells.

The integrity of the EBM is required for corneal epithelial cell homeostasis and recovery after wounding (Medeiros et al., 2018; Santhanam et al., 2017; Stramer et al., 2003; Torricelli et al., 2013). Numerous studies have focused on the ability of proteins secreted by corneal epithelial cells to induce changes in protein expression in stromal cells (Stramer et al., 2003; Torricelli et al., 2013). It is also clear that stromal cells secrete ECM proteins, including perlecan and nidogen-2 (Torricelli et al., 2015), that are components of the EBM, as well as growth factors that regulate epithelial corneal wound repair (Miyagi et al., 2018; Omoto et al., 2017). While our data suggests that stromal cells also secrete axon targeting molecules that diffuse into the epithelium to maintain ICBNs at their basal location within the epithelium, additional studies are necessary to determine if this is the case.

4.6. Future directions

FIB-SEM is a powerful technique to visualize the ultrastructure that exists within cells and to generate new insight into how cells are interacting with one another and their environment. Few studies have been published using this method to assess stratified squamous epithelia. The two studies that have been published on the skin describe lamellar granules (den Hollander et al., 2016; Yamanishi et al., 2019). The study by Courson and

colleagues (Courson et al., 2019) is the first we are aware of to look at the ICNs in the cornea using a related technique called serial block face imaging (SBFI). Our report is the first to look at how the ICNs respond to injury using FIB-SEM. While FIB-SEM is powerful, it takes time to sort out the correct fixation and mounting procedures needed to properly visualize the nerves within the tissue. The files generated using this approach are large and challenging to use to generate 3D volumes and to rotate them. Yet, new tools are being developed to facilitate analysis of FIB-SEM data sets. The serial image stacks we have generated here will be available to allow additional data analysis.

Supplementary Material

Refer to Web version on PubMed Central for supplementary material.

Acknowledgements

The FIB-SEM work described here was performed at the GW Nanofabrication and Imaging Center (NIC) at the GW School of Medicine and Health Sciences and funded by the GW Office of the Vice President for Research at the GW Science and Engineering Hall. The FIB-SEM and Arivis data was generated by Dr. Parlanti while at GWU before moving to her current position at Rutgers. Confocal imaging was supported by an equipment grant from the NIH S10 RR025565. The research described here was funded by NIH NEI EY8512 (MAS).

References

- Acosta MC, Tan ME, Belmonte C, Gallar J, 2001. Sensations evoked by selective mechanical, chemical, and thermal stimulation of the conjunctiva and cornea. *Invest. Ophthalmol. Vis. Sci* 42, 2063–2067. [PubMed: 11481273]
- Almasieh M, Wilson AM, Morquette B, Cueva Vargas JL, Di Polo A, 2012. The molecular basis of retinal ganglion cell death in glaucoma. *Prog. Retin. Eye Res* 31, 152–181. 10.1016/j.preteyeres.2011.11.002. [PubMed: 22155051]
- Asundi VK, Erdman R, Stahl RC, Carey DJ, 2003. Matrix metalloproteinase-dependent shedding of syndecan-3, a transmembrane heparan sulfate proteoglycan, in Schwann cells. *J. Neurosci. Res* 73, 593–602. 10.1002/jnr.10699. [PubMed: 12929127]
- Belmonte C, GarciaHirschfeld J, Gallar J, 1997. Neurobiology of ocular pain. *Prog. Retin. Eye Res* 16, 117–156. 10.1016/S1350-9462(96)00027-4.
- Berzat A, Hall A, 2010. Cellular responses to extracellular guidance cues. *EMBO J.* 29, 2734–2745. 10.1038/emboj.2010.170. [PubMed: 20717143]
- Beuerman RW, Rozsa AJ, 1984. Collateral sprouts are replaced by regenerating neurites in the wounded corneal epithelium. *Neurosci. Lett* 44, 99–104. 10.1016/0304-3940(84)90228-3. [PubMed: 6717860]
- Brines M, Culver DA, Ferdousi M, Tannemaat MR, van Velzen M, Dahan A, Malik RA, 2018. Corneal nerve fiber size adds utility to the diagnosis and assessment of therapeutic response in patients with small fiber neuropathy. *Sci. Rep* 8, 4734. 10.1038/s41598-018-23107-w. [PubMed: 29549285]
- Buommino E, Di Domenico M, Paoletti I, Fusco A, De Gregorio V, Cozza V, Rizzo A, Tufano MA, Donnarumma G, 2014. AlphaVBeta5 integrins mediates *Pseudomonas fluorescens* interaction with A549 cells. *Front. Biosci* 19, 408–415. 10.2741/4215.
- Courson JA, Smith I, Do T, Landry PT, Hargrave A, Behzad AR, Hanlon SD, Rumbaut RE, Smith CW, Burns AR, 2019. Serial block-face scanning electron microscopy reveals neuronal-epithelial cell fusion in the mouse cornea. *PLoS One* 14, e0224434. 10.1371/journal.pone.0224434.
- Court FA, Coleman MP, 2012. Mitochondria as a central sensor for axonal degenerative stimuli. *Trends Neurosci.* 35, 364–372. 10.1016/j.tins.2012.04.001. [PubMed: 22578891]
- Cruzat A, Qazi Y, Hamrah P, 2017. In vivo confocal microscopy of corneal nerves in health and disease. *Ocul. Surf* 15, 15–47. 10.1016/j.jtos.2016.09.004. [PubMed: 27771327]

- de Bruijn WC, 1973. Glycogen, its chemistry and morphologic appearance in the electron microscope. I. A modified OsO₄ fixative which selectively contrasts glycogen. *J Ultrastruct Res* 42, 29–50. 10.1016/s0022-5320(73)80004-8. [PubMed: 4567407]
- De Silva MEH, Zhang AC, Karahalios A, Chinnery HR, Downie LE, 2017. Laser scanning in vivo confocal microscopy (IVCM) for evaluating human corneal sub-basal nerve plexus parameters: protocol for a systematic review. *BMJ Open* 7, e018646. 10.1136/bmjopen-2017-018646.
- Deerincq TJ, 2010. NCMIR Methods for 3D EM: A New Protocol for Preparation of Biological Specimens for Serial Block Face Scanning Electron Microscopy.
- den Hollander L, Han H, de Winter M, Svensson L, Masich S, Daneholt B, Norlen L, 2016. Skin lamellar bodies are not discrete vesicles but part of a tubuloreticular network. *Acta Derm. Venereol* 96, 303–308. 10.2340/000155552249. [PubMed: 26439096]
- Dieckmann G, Goyal S, Hamrah P, 2017. Neuropathic corneal pain: approaches for management. *Ophthalmology* 124, S34–S47. 10.1016/j.ophtha.2017.08.004. [PubMed: 29055360]
- Fakih D, Zhao Z, Nicolle P, Reboussin E, Joubert F, Luzu J, Labbe A, Rostene W, Baudouin C, Melik Parsadaniantz S, Reaux-Le Goazigo A, 2019. Chronic dry eye induced corneal hypersensitivity, neuroinflammatory responses, and synaptic plasticity in the mouse trigeminal brainstem. *J. Neuroinflammation* 16, 268. 10.1186/s12974-019-1656-4. [PubMed: 31847868]
- Ferrari G, Chauhan SK, Ueno H, Nallasamy N, Gandolfi S, Borges L, Dana R, 2011. A novel mouse model for neurotrophic keratopathy: trigeminal nerve stereotactic electrolysis through the brain. *Invest. Ophthalmol. Vis. Sci* 52, 2532–2539. 10.1167/iovs.10-5688. [PubMed: 21071731]
- Flatters SJ, 2015. The contribution of mitochondria to sensory processing and pain. *Prog Mol Biol Transl Sci* 131, 119–146. 10.1016/bs.pmbts.2014.12.004. [PubMed: 25744672]
- Fleiszig SM, Zaidi TS, Pier GB, 1995. *Pseudomonas aeruginosa* invasion of and multiplication within corneal epithelial cells in vitro. *Infect. Immun* 63, 4072–4077. [PubMed: 7558321]
- Galluzzi L, Vitale I, Aaronson SA, Abrams JM, Adam D, Agostinis P, Alnemri ES, Altucci L, Amelio I, Andrews DW, Annicchiarico-Petruzzelli M, Antonov AV, Arama E, Baehrecke EH, Barlev NA, Bazan NG, Bernassola F, Bertrand MJM, Bianchi K, Blagosklonny MV, Blomgren K, Borner C, Boya P, Brenner C, Campanella M, Candi E, Carmona-Gutierrez D, Cecconi F, Chan FK, Chandel NS, Cheng EH, Chipuk JE, Cidlowski JA, Ciechanover A, Cohen GM, Conrad M, Cubillos-Ruiz JR, Czabotar PE, D'Angiolella V, Dawson TM, Dawson VL, De Laurenzi V, De Maria R, Debatin KM, DeBerardinis RJ, Deshmukh M, Di Daniele N, Di Virgilio F, Dixit VM, Dixon SJ, Duckett CS, Dynlacht BD, El-Deiry WS, Elrod JW, Fimia GM, Fulda S, Garcia-Saez AJ, Garg AD, Garrido C, Gavathiotis E, Golstein P, Gottlieb E, Green DR, Greene LA, Gronemeyer H, Gross A, Hajnoczky G, Hardwick JM, Harris IS, Hengartner MO, Hetz C, Ichijo H, Jaattela M, Joseph B, Jost PJ, Juin PP, Kaiser WJ, Karin M, Kaufmann T, Kepp O, Kimchi A, Kitsis RN, Klionsky J, Knight RA, Kumar S, Lee SW, Lemasters JJ, Levine B, Linkermann A, Lipton SA, Lockshin RA, Lopez-Otin C, Lowe SW, Luedde T, Lugli E, MacFarlane M, Madeo F, Malewicz M, Malorni W, Manic G, Marine JC, Martin SJ, Martinou JC, Medema JP, Mehlen P, Meier P, Melino S, Miao A, Molkentin JD, Moll UM, Munoz-Pinedo C, Nagata S, Nunez G, Oberst A, Oren M, Overholtzer M, Pagano M, Panaretakis T, Pasparakis M, Penninger JM, Pereira DM, Pervaiz S, Peter ME, Piacentini M, Pinton P, Prehn JHM, Puthalakath H, Rabinovich GA, Rehm M, Rizzuto R, Rodrigues CMP, Rubinsztein DC, Rudel T, Ryan KM, Sayan E, Scorrano L, Shao F, Shi Y, Silke J, Simon HU, Sistigu A, Stockwell BR, Strasser A, Szabadkai G, Tait SWG, Tang D, Tavernarakis N, Thorburn A, Tsujimoto Y, Turk B, Vanden Berghe T, Vandenabeele P, Vander Heiden MG, Villunger A, Virgin HW, Vousden KH, Vucic D, Wagner EF, Walczak H, Wallach D, Wang Y, Wells JA, Wood W, Yuan J, Zakeri Z, Zhivotovsky B, Zitvogel L, Melino G, Kroemer G, 2018. Molecular mechanisms of cell death: recommendations of the nomenclature committee on cell death 2018. *Cell Death Differ* 25, 486–541. 10.1038/s41418-017-0012-4. [PubMed: 29362479]
- Gao N, Yan C, Lee P, Sun H, Yu FS, 2016. Dendritic cell dysfunction and diabetic sensory neuropathy in the cornea. *J. Clin. Invest* 126, 1998–2011. 10.1172/JCI85097. [PubMed: 27064280]
- Goutebroze L, Carnaud M, Denisenko N, Bouterin MC, Girault JA, 2003. Syndecan-3 and syndecan-4 are enriched in Schwann cell perinodal processes. *BMC Neurosci* 4, 29. 10.1186/1471-2202-4-29. [PubMed: 14622446]
- Gumy LF, Tan CL, Fawcett JW, 2010. The role of local protein synthesis and degradation in axon regeneration. *Exp. Neurol* 223, 28–37. 10.1016/j.expneurol.2009.06.004. [PubMed: 19520073]

- Hamid HS, Mervak CM, Munch AE, Robell NJ, Hayes JM, Porzio MT, Singleton JR, Smith AG, Feldman EL, Lentz SI, 2014. Hyperglycemia- and neuropathy-induced changes in mitochondria within sensory nerves. *Ann Clin Transl Neurol* 1, 799–812. 10.1002/acn3.119. [PubMed: 25493271]
- Hamrah P, Dana MR, 2007. Corneal antigen-presenting cells. *Chem. Immunol. Allergy* 92, 58–70. 10.1159/000099254. [PubMed: 17264483]
- Hamrah P, Qazi Y, Shahatit B, Dastjerdi MH, Pavan-Langston D, Jacobs DS, Rosenthal P, 2017. Corneal nerve and epithelial cell alterations in corneal allodynia: an in vivo confocal microscopy case series. *Ocul. Surf* 15, 139–151. 10.1016/j.jtos.2016.10.002. [PubMed: 27816571]
- Hayashi A, Naseri A, Pennesi ME, de Juan E Jr., 2009. Subretinal delivery of immunoglobulin G with gold nanoparticles in the rabbit eye. *Jpn. J. Ophthalmol* 53, 249–256. 10.1007/s10384-009-0655-x. [PubMed: 19484444]
- Ishibashi F, Kojima R, Taniguchi M, Kosaka A, Uetake H, Tavakoli M, 2016. The expanded bead size of corneal C-nerve fibers visualized by corneal confocal microscopy is associated with slow conduction velocity of the peripheral nerves in patients with type 2 diabetes mellitus. *J Diabetes Res* 2016, 3653459. 10.1155/2016/3653459.
- Jiang N, Rasmussen JP, Clanton JA, Rosenberg MF, Luedke KP, Cronan MR, Parker ED, Kim HJ, Vaughan JC, Sagasti A, Parrish JZ, 2019. A conserved morphogenetic mechanism for epidermal ensheathment of nociceptive sensory neurites. *Elife* 8. 10.7554/eLife.42455.
- Jiao H, Naranjo Golborne C, Dando SJ, McMenamin PG, Downie LE, Chinnery HR, 2019. Topographical and morphological differences of corneal dendritic cells during steady state and inflammation. *Ocul. Immunol. Inflamm* 1, 10. 10.1080/09273948.2019.1646775.
- Jorgens DM, Inman JL, Wojcik M, Robertson C, Palsdottir H, Tsai WT, Huang H, Bruni-Cardoso A, Lopez CS, Bissell MJ, Xu K, Auer M, 2017. Deep nuclear invaginations are linked to cytoskeletal filaments - integrated bioimaging of epithelial cells in 3D culture. *J. Cell Sci* 130, 177–189. 10.1242/jcs.190967. [PubMed: 27505896]
- Kerrigan-Baumrind LA, Quigley HA, Pease ME, Kerrigan DF, Mitchell RS, 2000. Number of ganglion cells in glaucoma eyes compared with threshold visual field tests in the same persons. *Invest. Ophthalmol. Vis. Sci* 41, 741–748. [PubMed: 10711689]
- Kevany BM, Palczewski K, 2010. Phagocytosis of retinal rod and cone photoreceptors. *Physiology* 25, 8–15. 10.1152/physiol.00038.2009. [PubMed: 20134024]
- Kheirkhah A, Rahimi Darabad R, Cruzat A, Hajrasouliha AR, Witkin D, Wong N, Dana R, Hamrah P, 2015. Corneal epithelial immune dendritic cell alterations in subtypes of dry eye disease: a pilot in vivo confocal microscopic study. *Invest. Ophthalmol. Vis. Sci* 56, 7179–7185. 10.1167/iovs.15-17433. [PubMed: 26540656]
- Kuwabara T, Perkins DG, Cogan DG, 1976. Sliding of the epithelium in experimental corneal wounds. *Invest. Ophthalmol* 15, 4–14. [PubMed: 1245378]
- Launay PS, Reboussin E, Liang H, Kessal K, Godefroy D, Rostene W, Sahel JA, Baudouin C, Melik Parsadaniantz S, Reaux Le Goazigo A, 2016. Ocular inflammation induces trigeminal pain, peripheral and central neuroinflammatory mechanisms. *Neurobiol. Dis* 88, 16–28. 10.1016/j.nbd.2015.12.017. [PubMed: 26747211]
- Lin SR, Aldave AJ, Chodosh J, 2019. Recurrent corneal erosion syndrome. *Br. J. Ophthalmol* 103, 1204–1208. 10.1136/bjophthalmol-2019-313835. [PubMed: 30760455]
- Luzio JP, Hackmann Y, Dieckmann NM, Griffiths GM, 2014. The biogenesis of lysosomes and lysosome-related organelles. *Cold Spring Harb Perspect Biol* 6, a016840. 10.1101/cshperspect.a016840.
- Lwigale PY, 2001. Embryonic origin of avian corneal sensory nerves. *Dev. Biol* 239, 323–337. 10.1006/dbio.2001.0450. [PubMed: 11784038]
- Marfurt CF, 1981. The central projections of trigeminal primary afferent neurons in the cat as determined by the transganglionic transport of horseradish peroxidase. *J. Comp. Neurol* 203, 785–798. 10.1002/cne.902030414. [PubMed: 6173403]
- Marfurt CF, Del Toro DR, 1987. Corneal sensory pathway in the rat: a horseradish peroxidase tracing study. *J. Comp. Neurol* 261, 450–459. 10.1002/cne.902610309. [PubMed: 3112189]

- Martinez S, Belmonte C, 1996. C-Fos expression in trigeminal nucleus neurons after chemical irritation of the cornea: reduction by selective blockade of nociceptor chemosensitivity. *Exp. Brain Res* 109, 56–62. 10.1007/bf00228626. [PubMed: 8740208]
- McKay TB, Seyed-Razavi Y, Ghezzi CE, Dieckmann G, Nieland TJJ, Cairns DM, Pollard RE, Hamrah P, Kaplan DL, 2019. Corneal pain and experimental model development. *Prog. Retin. Eye Res* 71, 88–113. 10.1016/j.preteyeres.2018.11.005. [PubMed: 30453079]
- Medeiros CS, Marino GK, Santhiago MR, Wilson SE, 2018. The corneal basement membranes and stromal fibrosis. *Invest. Ophthalmol. Vis. Sci* 59, 4044–4053. 10.1167/iovs.18-24428. [PubMed: 30098200]
- Miller DD, Hasan SA, Simmons NL, Stewart MW, 2019. Recurrent corneal erosion: a comprehensive review. *Clin. Ophthalmol* 13, 325–335. 10.2147/OPTH.S157430. [PubMed: 30809089]
- Miyagi H, Thomasy SM, Russell P, Murphy CJ, 2018. The role of hepatocyte growth factor in corneal wound healing. *Exp. Eye Res* 166, 49–55. 10.1016/j.exer.2017.10.006. [PubMed: 29024692]
- Muller LJ, Marfurt CF, Kruse F, Tervo TM, 2003. Corneal nerves: structure, contents and function. *Exp. Eye Res* 76, 521–542. 10.1016/s00144835(03)00050-2. [PubMed: 12697417]
- Muller LJ, Pels L, Vrensen GF, 1996. Ultrastructural organization of human corneal nerves. *Invest. Ophthalmol. Vis. Sci* 37, 476–488. [PubMed: 8595948]
- Muller LJ, Vrensen GF, Pels L, Cardozo BN, Willekens B, 1997. Architecture of human corneal nerves. *Invest. Ophthalmol. Vis. Sci* 38, 985–994. [PubMed: 9112994]
- Myers JP, Santiago-Medina M, Gomez TM, 2011. Regulation of axonal outgrowth and pathfinding by integrin-ECM interactions. *Dev Neurobiol* 71, 901–923. 10.1002/dneu.20931. [PubMed: 21714101]
- Nakamura A, Hayakawa T, Kuwahara S, Maeda S, Tanaka K, Seki M, Mimura O, 2007. Morphological and immunohistochemical characterization of the trigeminal ganglion neurons innervating the cornea and upper eyelid of the rat. *J. Chem. Neuroanat* 34, 95–101. 10.1016/j.jchemneu.2007.05.005. [PubMed: 17587545]
- Niederhorn JY, Peeler JS, Mellon J, 1989. Phagocytosis of particulate antigens by corneal epithelial cells stimulates interleukin-1 secretion and migration of Langerhans cells into the central cornea. *Reg. Immunol* 2, 83–90. [PubMed: 2641920]
- O'Donnell M, Chance RK, Bashaw GJ, 2009. Axon growth and guidance: receptor regulation and signal transduction. *Annu. Rev. Neurosci* 32, 383–412. 10.1146/annurev.neuro.051508.135614. [PubMed: 19400716]
- Ogita S, 1978. [Histoenzymic chemistry study of irradiated rabbit corneas using microspectrophotometry (author's transl)]. *Nippon. Ganka Gakkai Zasshi* 82, 208–218. [PubMed: 676932]
- Omoto M, Suri K, Amouzegar A, Li M, Katikireddy KR, Mittal SK, Chauhan SK, 2017. Hepatocyte growth factor suppresses inflammation and promotes epithelium repair in corneal injury. *Mol. Ther* 25, 1881–1888. 10.1016/j.ymthe.2017.04.020. [PubMed: 28502469]
- Pajoohesh-Ganji A, Pal-Ghosh S, Tadvalkar G, Kyne BM, Saban DR, Stepp MA, 2015. Partial denervation of sub-basal axons persists following debridement wounds to the mouse cornea. *Lab. Invest* 95, 1305–1318. 10.1038/labinvest.2015.113. [PubMed: 26280222]
- Pal-Ghosh S, Pajoohesh-Ganji A, Menko AS, Oh HY, Tadvalkar G, Saban DR, Stepp MA, 2014. Cytokine deposition alters leukocyte morphology and initial recruitment of monocytes and gammadeltaT cells after corneal injury. *Invest. Ophthalmol. Vis. Sci* 55, 2757–2765. 10.1167/iovs.13-13557. [PubMed: 24677104]
- Pal-Ghosh S, Tadvalkar G, Stepp MA, 2017. Alterations in corneal sensory nerves during homeostasis, aging, and after injury in mice lacking the heparan sulfate proteoglycan syndecan-1. *Invest. Ophthalmol. Vis. Sci* 58, 4959–4975. 10.1167/iovs.17-21531. [PubMed: 28973369]
- Parlanti P, Cappello V, Brun F, Tromba G, Rigolio R, Tonazzini I, Cecchini M, Piazza V, Gemmi M, 2017. Size and specimen-dependent strategy for x-ray microct and tem correlative analysis of nervous system samples. *Sci. Rep* 7, 2858. 10.1038/s41598-017-02998-1. [PubMed: 28588216]
- Parlanti P, Rigolio R, Tromba G, Manzini C, 2019. Correlative Synchrotron Micro-CT and FIB-SEM Imaging for the Analysis of Multifocal Pathologies.

- Patel DV, McGhee CN, 2005. Mapping of the normal human corneal sub-Basal nerve plexus by in vivo laser scanning confocal microscopy. *Invest. Ophthalmol. Vis. Sci* 46, 4485–4488. 10.1167/iovs.05-0794. [PubMed: 16303938]
- Peddie CJ, Collinson LM, 2014. Exploring the third dimension: volume electron microscopy comes of age. *Micron* 61, 9–19. 10.1016/j.micron.2014.01.009. [PubMed: 24792442]
- Randles MJ, Humphries MJ, Lennon R, 2017. Proteomic definitions of basement membrane composition in health and disease. *Matrix Biol.* 57–58, 12–28. 10.1016/j.matbio.2016.08.006. [PubMed: 27553508]
- Rasmussen JP, Sack GS, Martin SM, Sagasti A, 2015. Vertebrate epidermal cells are broad-specificity phagocytes that clear sensory axon debris. *J. Neurosci* 35, 559–570. 10.1523/JNEUROSCI.3613-14.2015. [PubMed: 25589751]
- Roggia MF, Ueta T, 2015. $\alpha 5$ integrin/FAK/PGC-1 α pathway confers protective effects on retinal pigment epithelium. *PloS One* 10, e0134870. 10.1371/journal.pone.0134870.
- Rozsa AJ, Beuerman RW, 1982. Density and organization of free nerve endings in the corneal epithelium of the rabbit. *Pain* 14, 105–120. 10.1016/0304-3959(82)90092-6. [PubMed: 7177676]
- Rozsa AJ, Guss RB, Beuerman RW, 1983. Neural remodeling following experimental surgery of the rabbit cornea. *Invest. Ophthalmol. Vis. Sci* 24, 1033–1051. [PubMed: 6874268]
- Saban DR, 2014. The chemokine receptor *CCR7* expressed by dendritic cells: a key player in corneal and ocular surface inflammation. *Ocul. Surf* 12, 87–99. 10.1016/j.jtos.2013.10.007. [PubMed: 24725321]
- Saftig P, Klumperman J, 2009. Lysosome biogenesis and lysosomal membrane proteins: trafficking meets function. *Nat. Rev. Mol. Cell Biol* 10, 623–635. 10.1038/nrm2745. [PubMed: 19672277]
- Santhanam A, Marino GK, Torricelli AA, Wilson SE, 2017. EBM regeneration and changes in EBM component mRNA expression in stromal cells after corneal injury. *Mol. Vis* 23, 39–51. [PubMed: 28275314]
- Schmidt RE, Parvin CA, Green KG, 2008. Synaptic ultrastructural alterations anticipate the development of neuroaxonal dystrophy in sympathetic ganglia of aged and diabetic mice. *J. Neuropathol. Exp. Neurol* 67, 1166–1186. 10.1097/NEN.0b013e318190d6db. [PubMed: 19018240]
- Seyed-Razavi Y, Lopez MJ, Mantopoulos D, Zheng L, Massberg S, Sendra VG, Harris DL, Hamrah P, 2019. Kinetics of corneal leukocytes by intravitreal multi-photon microscopy. *FASEB J* 33, 2199–2211. 10.1096/fj.201800684RR. [PubMed: 30226811]
- Shaheen BS, Bakir M, Jain S, 2014. Corneal nerves in health and disease. *Surv. Ophthalmol* 59, 263–285. 10.1016/j.survophthal.2013.09.002. [PubMed: 24461367]
- Shimajima M, Yuasa S, Motoda C, Yozu G, Nagai T, Ito S, Lachmann M, Kashimura S, Takei M, Kusumoto D, Kunitomi A, Hayashiji N, Seki T, Tohyama S, Hashimoto H, Kodaira M, Egashira T, Hayashi K, Nakanishi C, Sakata K, Yamagishi M, Fukuda K, 2017. Emerin plays a crucial role in nuclear invagination and in the nuclear calcium transient. *Sci. Rep* 7, 44312. 10.1038/srep44312. [PubMed: 28290476]
- Stapp MA, Pal-Ghosh S, Downie LE, Zhang CC, Chinnery HR, Mchet J, Di Girolamo A, 2020. Corneal epithelial neuromas: a case of mistaken identity? (The work). *Cornea*. 10.1097/ICO.0000000000002294.
- Stapp MA, Pal-Ghosh S, Tadvalkar G, Li L, Brooks SR, Morasso MI, 2018. Molecular basis of Mitomycin C enhanced corneal sensory nerve repair after debridement wounding. *Sci. Rep* 8, 16960. 10.1038/s41598-01835090-3. [PubMed: 30446696]
- Stapp MA, Spurr-Michaud S, Tisdale A, Elwell J, Gipson IK, 1990. Alpha 6 beta 4 integrin heterodimer is a component of hemidesmosomes. *Proc. Natl. Acad. Sci. U. S. A* 87, 8970–8974. 10.1073/pnas.87.22.8970. [PubMed: 2247472]
- Stapp MA, Tadvalkar G, Hakh R, Pal-Ghosh S, 2017. Corneal epithelial cells function as surrogate Schwann cells for their sensory nerves. *Glia* 65, 851–863. 10.1002/glia.23102. [PubMed: 27878997]
- Stramer BM, Zieske JD, Jung JC, Austin JS, Fini ME, 2003. Molecular mechanisms controlling the fibrotic repair phenotype in cornea: implications for surgical outcomes. *Invest. Ophthalmol. Vis. Sci* 44, 4237–4246. 10.1167/iovs.02-1188. [PubMed: 14507867]

- Tenenbaum CM, Misra M, Alizzi RA, Gavis ER, 2017. Enclosure of dendrites by epidermal cells restricts branching and permits coordinated development of spatially overlapping sensory neurons. *Cell Rep.* 20, 3043–3056. 10.1016/j.celrep.2017.09.001. [PubMed: 28954223]
- Tervo T, Holopainen J, Belmonte C, 2016. Confocal microscopy of corneal nerves—a limited but still useful technique to evaluate peripheral neuropathies. *JAMA Ophthalmol* 134, 990–991. 10.1001/jamaophthalmol.2016.2178. [PubMed: 27368077]
- Torricelli AA, Marino GK, Santhanam A, Wu J, Singh A, Wilson SE, 2015. Epithelial basement membrane proteins perlecan and nidogen-2 are up-regulated in stromal cells after epithelial injury in human corneas. *Exp. Eye Res* 134, 33–38. 10.1016/j.exer.2015.03.016. [PubMed: 25797478]
- Torricelli AA, Singh V, Santhiago MR, Wilson SE, 2013. The corneal epithelial basement membrane: structure, function, and disease. *Invest. Ophthalmol. Vis. Sci* 54, 6390–6400. 10.1167/iovs.13-12547. [PubMed: 24078382]
- Uhler C, Shivashankar GV, 2017. Regulation of genome organization and gene expression by nuclear mechanotransduction. *Nat. Rev. Mol. Cell Biol* 18, 717–727. 10.1038/nrm.2017.101. [PubMed: 29044247]
- Valyi-Nagy T, Deshmane S, Dillner A, Fraser NW, 1991. Induction of cellular transcription factors in trigeminal ganglia of mice by corneal scarification, herpes simplex virus type 1 infection, and explantation of trigeminal ganglia. *J. Virol* 65, 4142–4152. [PubMed: 1649322]
- Villani E, Baudouin C, Efron N, Hamrah P, Kojima T, Patel SV, Pflugfelder SC, Zhivov A, Dogru M, 2014. In vivo confocal microscopy of the ocular surface: from bench to bedside. *Curr. Eye Res* 39, 213–231. 10.3109/02713683.2013.842592. [PubMed: 24215436]
- Villegas R, Martinez NW, Lillo J, Pihan P, Hernandez D, Twiss JL, Court FA, 2014. Calcium release from intra-axonal endoplasmic reticulum leads to axon degeneration through mitochondrial dysfunction. *J. Neurosci* 34, 7179–7189. 10.1523/JNEUROSCI.4784-13.2014. [PubMed: 24849352]
- Watson SL, Leung V, 2018. Interventions for recurrent corneal erosions. *Cochrane Database Syst. Rev* 7, CD001861. 10.1002/14651858.CD001861.pub4.
- Yamanishi H, Soma T, Kishimoto J, Hibino T, Ishida-Yamamoto A, 2019. Marked changes in lamellar granule and trans-golgi network structure occur during epidermal keratinocyte differentiation. *J. Invest. Dermatol* 139, 352–359. 10.1016/j.jid.2018.07.043. [PubMed: 30240698]

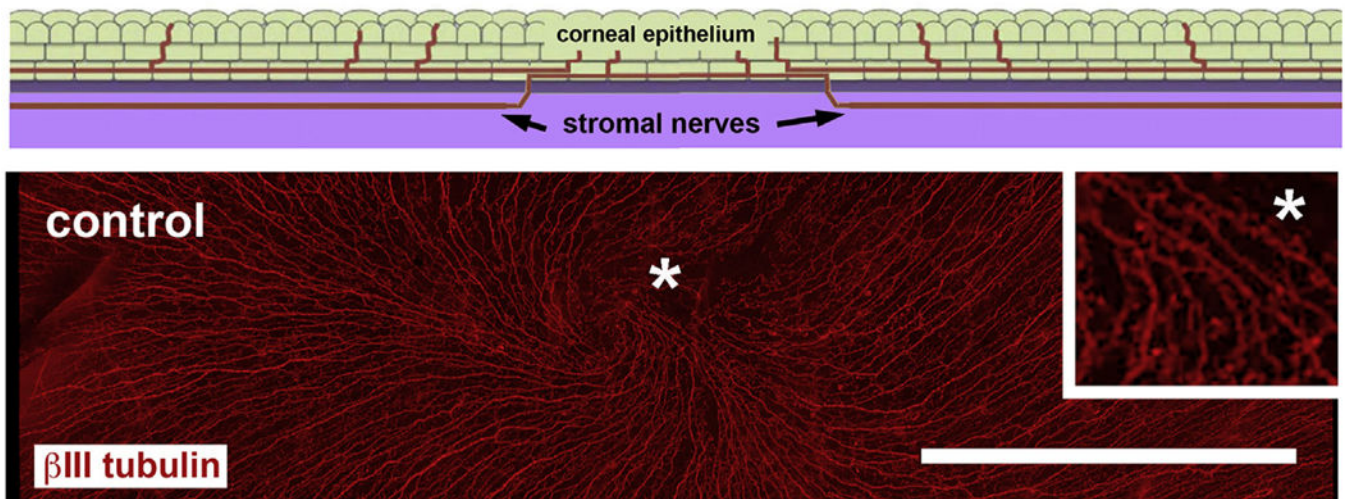


Fig. 1. Intraepithelial corneal nerves (ICNs) run parallel to the ocular surface and form a vortex at the corneal center.

The schematic image shows a cross sectional view through an unwounded cornea highlighting the fact that the ICNs (red) enter the corneal epithelium (green) from the stroma (lilac) and extend parallel to the basement membrane (grey). The ICNs consist of intraepithelial corneal basal nerves (ICBNs), localized at the basal aspect of the basal cells, as well as the intraepithelial corneal nerve terminals (ICNTs). Below the schematic is an en face image showing β III tubulin expressing ICNs in the corneal epithelium extending from the periphery towards the corneal center terminating at the vortex. The inset on the right shows the area near the vortex indicated by the asterisk after being magnified 4 \times . Bar =500 μ M. (For interpretation of the references to color in this figure legend, the reader is referred to the Web version of this article.)

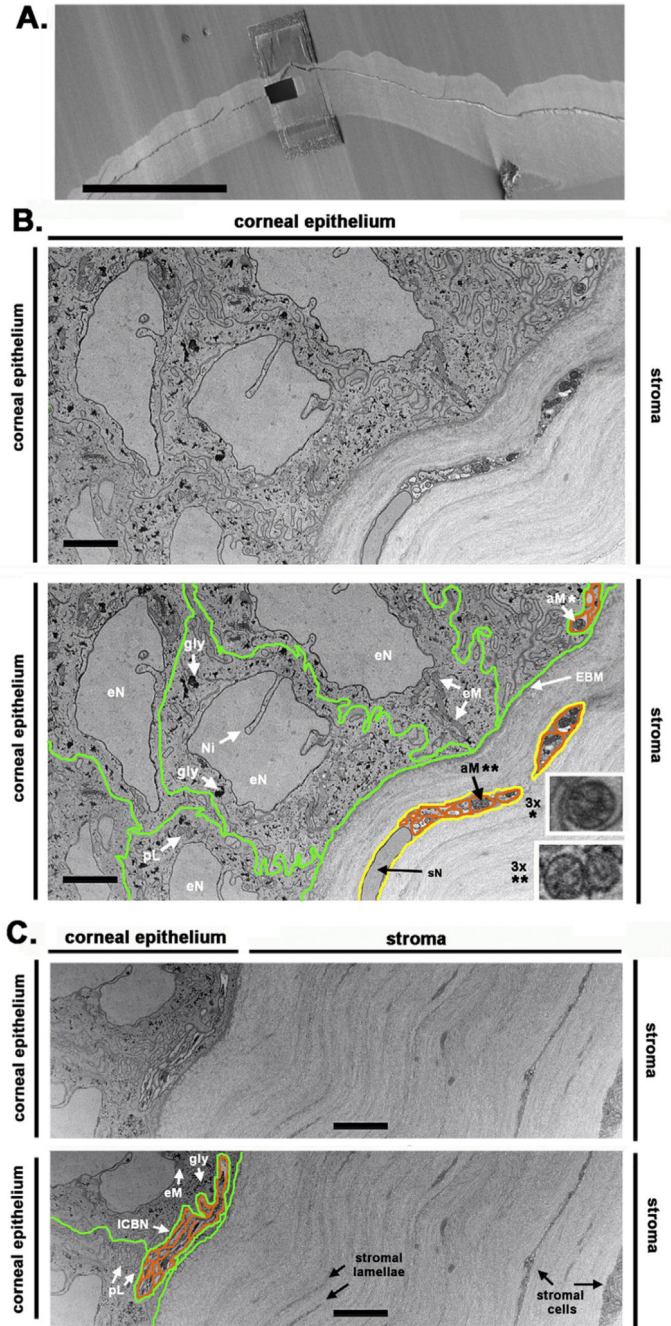


Fig. 2. FIB-SEM reveals ICBNs within corneal epithelial basal cells.

A. The unwounded mouse cornea is shown mounted prior to milling and serial sectioning. The site where the trench will be milled is shown. Representative duplicate images obtained from a control cornea at the epithelial: stromal interface are shown in **B** and **C**. The duplicate images are labeled and the corneal epithelial cell membrane, ICN axonal membrane are also indicated. Schwann cells are shown in both B and C; the images below have numerous structures and organelles labeled. Note the clusters of ICBNs located above the basement membrane at the far right in B and center in C. Axonal mitochondria from

the ICBN (*) and a stromal nerve (**) in B were digitally magnified 3× and presented in the insets to better show their cristae. ICBNs = intraepithelial corneal basal nerves, eN = epithelial cell nucleus, Ni = nuclear invagination, sN = Schwann cell nucleus, gly = glycogen, aM = axonal mitochondria, eM = epithelial cell mitochondria, EBM = epithelial basement membrane, pL = putative primary lysosome. Epithelial cell membranes are highlighted in green, axonal membranes highlighted in orange, and Schwann cell membranes are highlighted in yellow. Supplemental movie 1 shows serial sections through the unwounded cornea. Bar in A = 400 μm and bars in B,C = 4 μm. (For interpretation of the references to color in this figure legend, the reader is referred to the Web version of this article.)

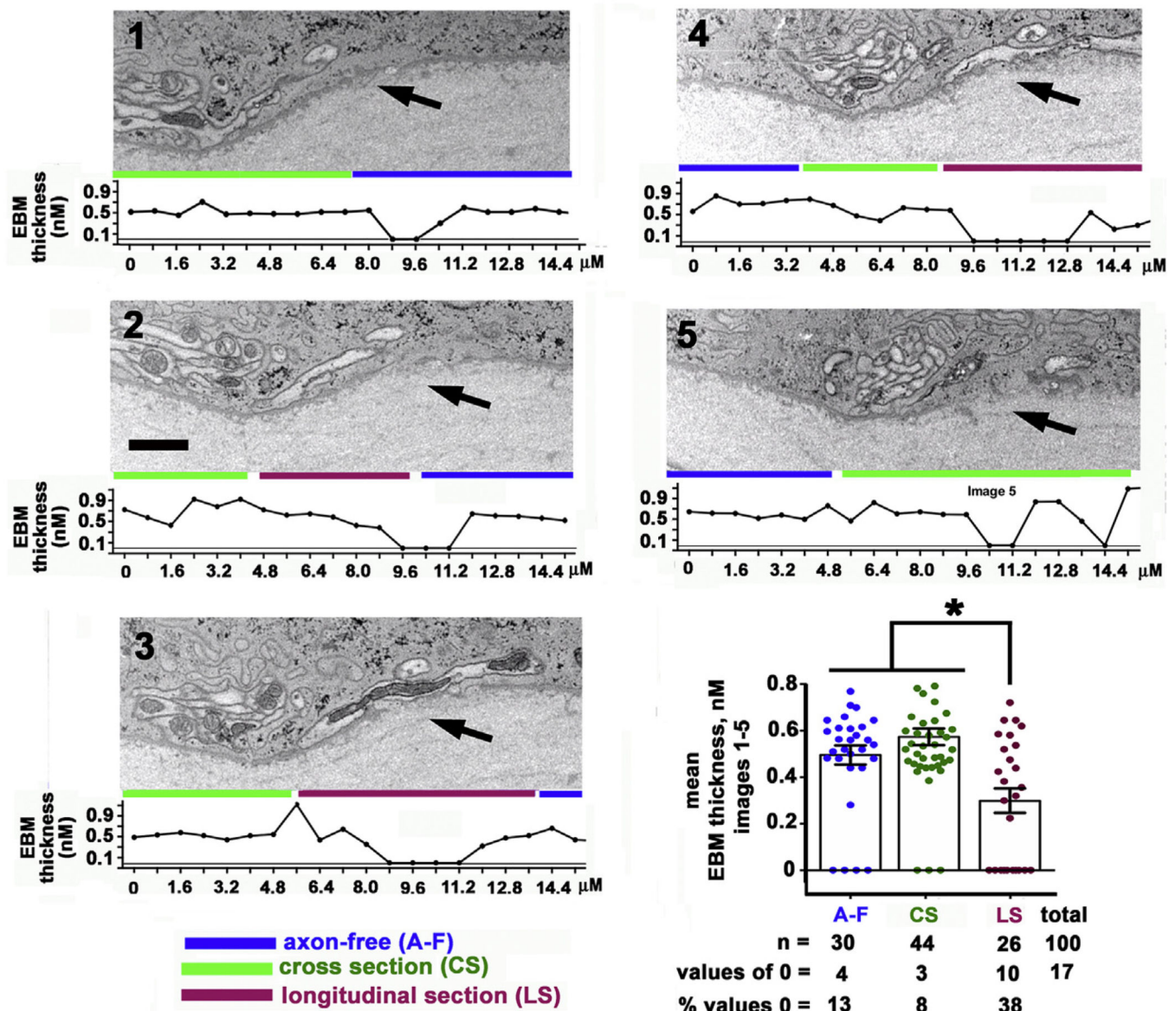


Fig. 3. The epithelial basement membrane (EBM) is thinner at sites where ICBNs are present. Serial FIB-SEM images (1–5) were obtained from an unwounded cornea showing the epithelial stroma interface. Arrows highlight sites where morphological changes in the EBM were observed. The thickness of the EBM was assessed along the epithelial: stromal interface on each of the five images assessed. Below each image is a graph showing the EBM thickness (nm) as a function of distance. 20 measurements were obtained for each image. EBM thickness values were clustered into 3 groups: areas that were axon-free (A-F; blue lines), areas with ICNs imaged in cross section (CS; green lines), and areas with ICBNs imaged in longitudinal section (LS; maroon lines). A graph of the mean EBM thickness for the three clusters is presented. EBM thickness is the same for axon-free and CS clusters but areas with ICBNs imaged in longitudinal section have significantly lower mean EBM

thickness. Bar =2 μm . (For interpretation of the references to color in this figure legend, the reader is referred to the Web version of this article.)

Author Manuscript

Author Manuscript

Author Manuscript

Author Manuscript

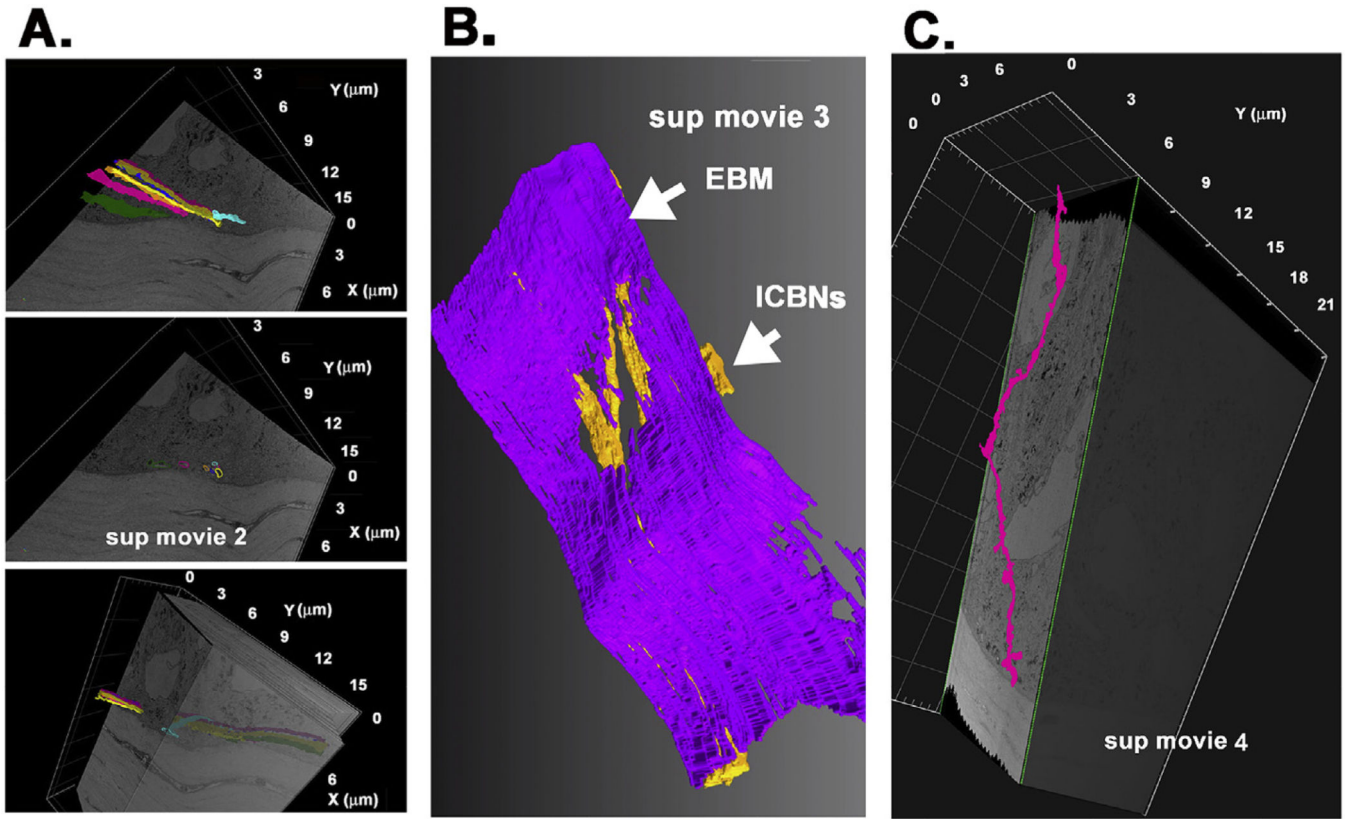


Fig. 4. Segmentation can be used to follow ICBNs and intraepithelial corneal nerve terminals (ICNTs) within the epithelium.

A. Segmentation shows an ICBN consisting of several individual axons above the EBM. One axon (aqua) moves in a different direction compared to the rest of the axons in the cluster shown. These panels were obtained from Supplemental Movie 2. **B.** Segmentation of the same area shown in A with all axons (yellow) and the EBM (purple) shows the thinning of the electron density in the EBM at sites where the ICBNs come in close contact with the basement membrane. The image shown was taken from Supplemental Movie 3. **C.** Segmentation shows an ICNT extending apically. ICNTs are thinner than ICBNs and tend to consist of only one or two axons. The ICNT shown has one axon. The image shown was taken from Supplemental Movie 4. (For interpretation of the references to color in this figure legend, the reader is referred to the Web version of this article.)

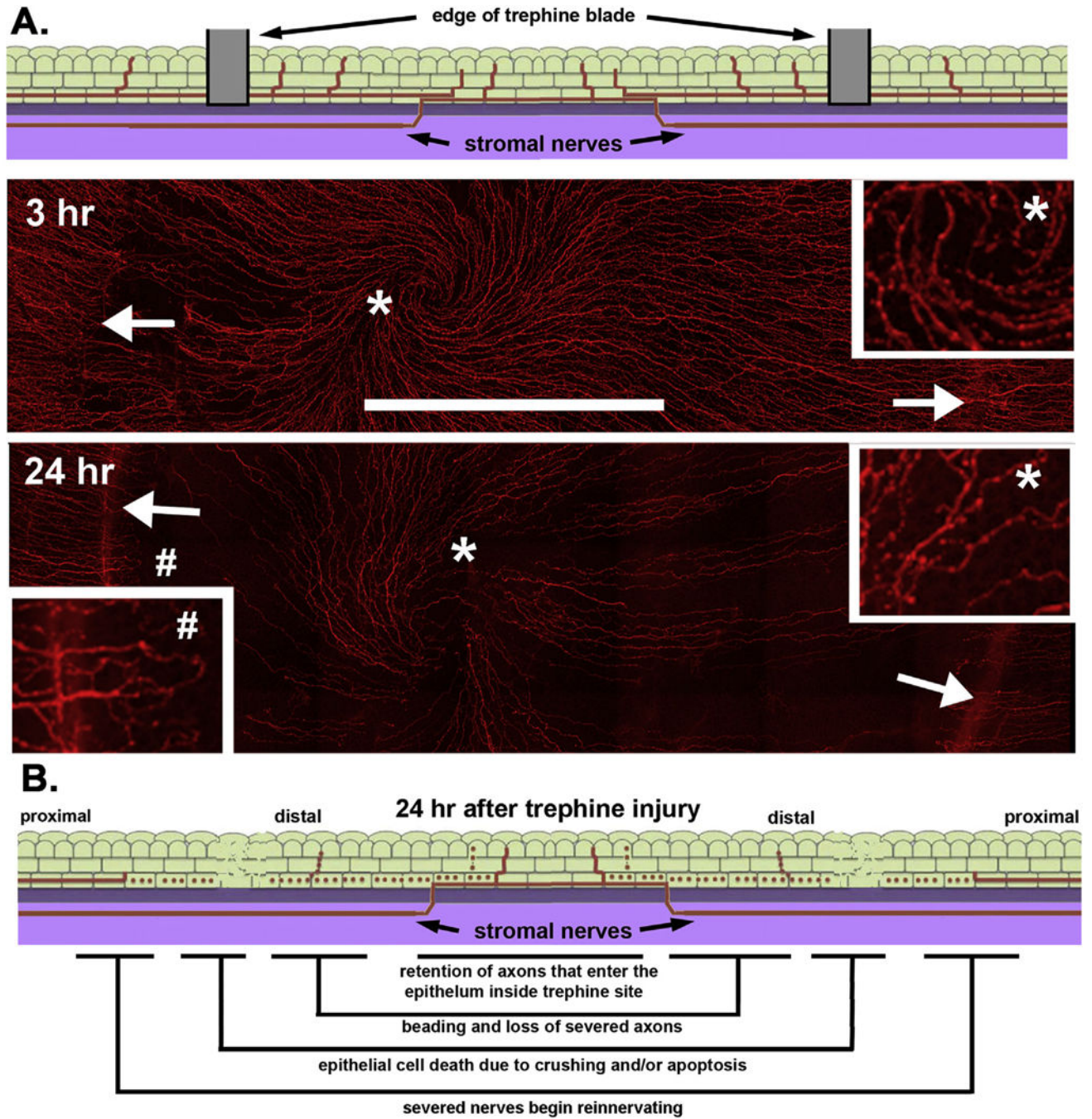


Fig. 5. Intraepithelial corneal nerves (ICNs) are partially denervated 24 h after trephine-only crush injury.

A. The schematic image at the top shows a cross section indicating where the 1.5 mm diameter trephine blade comes in contact with the corneal surface where it severs or crushes the axons. Below are representative *en face* confocal images of whole mount mouse corneas showing ICNs at 3 and 24hr after trephine injury; the sites where the trephine blade came in contact with the corneal surface are indicated by arrows. The inset on the right shows the area near the vortex indicated by the asterisk after being magnified 4×. Compared to controls

in Fig. 1, fewer axons with more beading are present. The inset on the left shows the area near the injury site indicated by a pound symbol (#) after being magnified 4×. Note that numerous axons proximal to the injury site can be seen extending towards the corneal center at 24h. **B.** The schematic image summarizes the changes that take place in the distal and proximal ICNs in the first 24h after trephine injury. Bar in A = 500 μm.

Author Manuscript

Author Manuscript

Author Manuscript

Author Manuscript

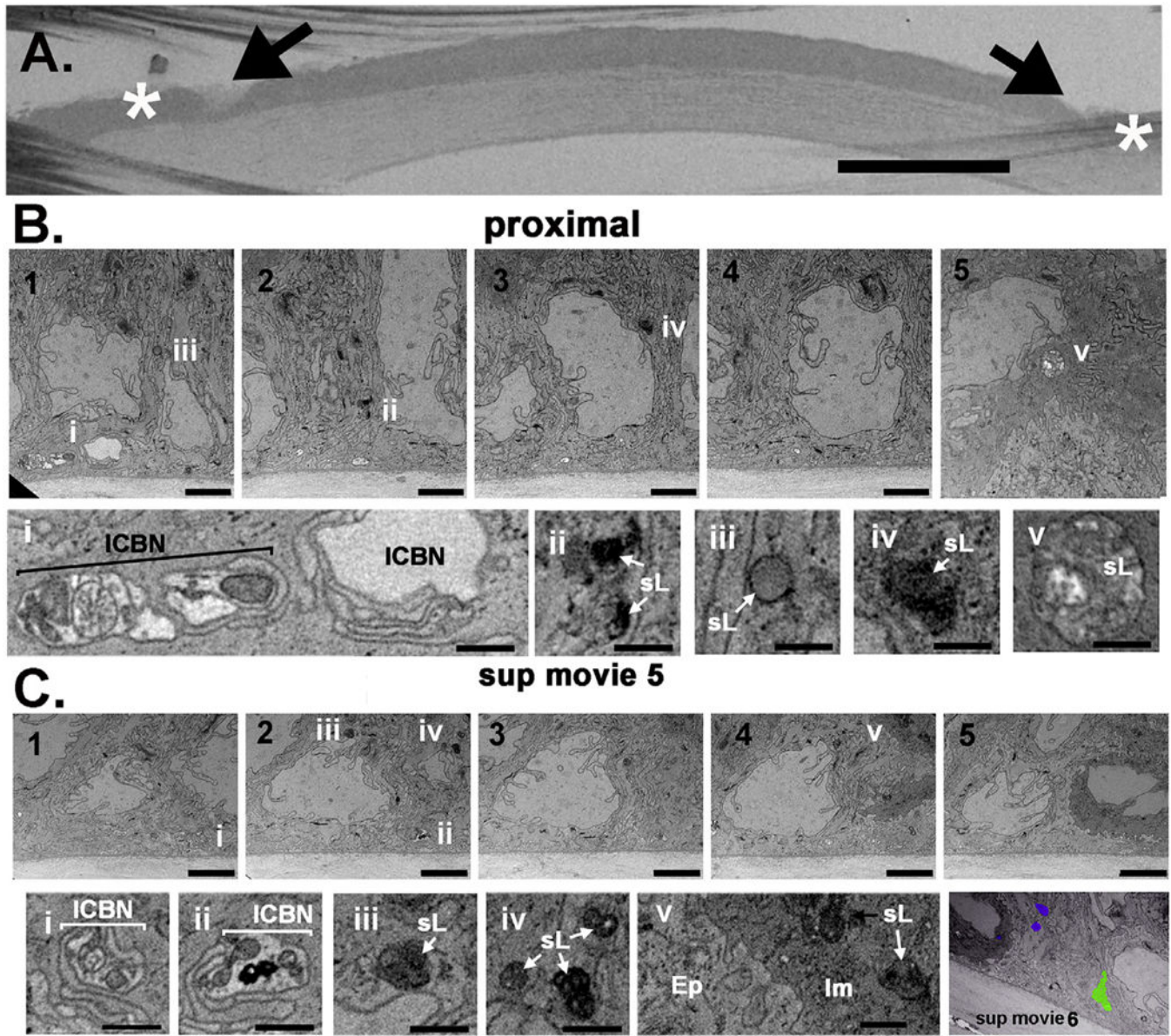


Fig. 6. Corneal epithelial basal cells proximal to the injury site contain electron dense organelles consistent with secondary lysosomes 3 h after trephine injury.
A. The trephine wounded mouse cornea is shown embedded and mounted on the block face. Arrows show sites where the trephine blade crushed or severed axons and asterisks indicate the sites where milling was performed. ICBNs proximal to the injury site are swollen and have varicosities. Bar in A = 400 μ m. **B and C.** Serial images obtained proximal to the injury site from a trephine wounded cornea at the epithelial: stromal interface are shown in images B1–5 and C1–5. Below, images Bi–v and Ci–v show higher magnification images highlighting features of interest. Supplemental Movie 5 shows the serial sections through the trephine wounded cornea that the images shown in B are obtained from. Bars in B and C are 2 μ m and bars in Bi–v and Ci–v are 500 nm. The final panel shown in C is an image taken from Supplemental Movie 6 that shows segmentation of an axon (green) and 3 lysosomes (purple) at a site proximal to the trephine injury. Two lysosomes are within the epithelium

whereas a third is located within the immune cell. The segmentation of the axon shows that it is swollen and has varicosities along its length. ICBN = intraepithelial corneal basal nerves, sL =secondary lysosomes, Im= immune cell, Ep =epithelial cell. (For interpretation of the references to color in this figure legend, the reader is referred to the Web version of this article.)

Author Manuscript

Author Manuscript

Author Manuscript

Author Manuscript

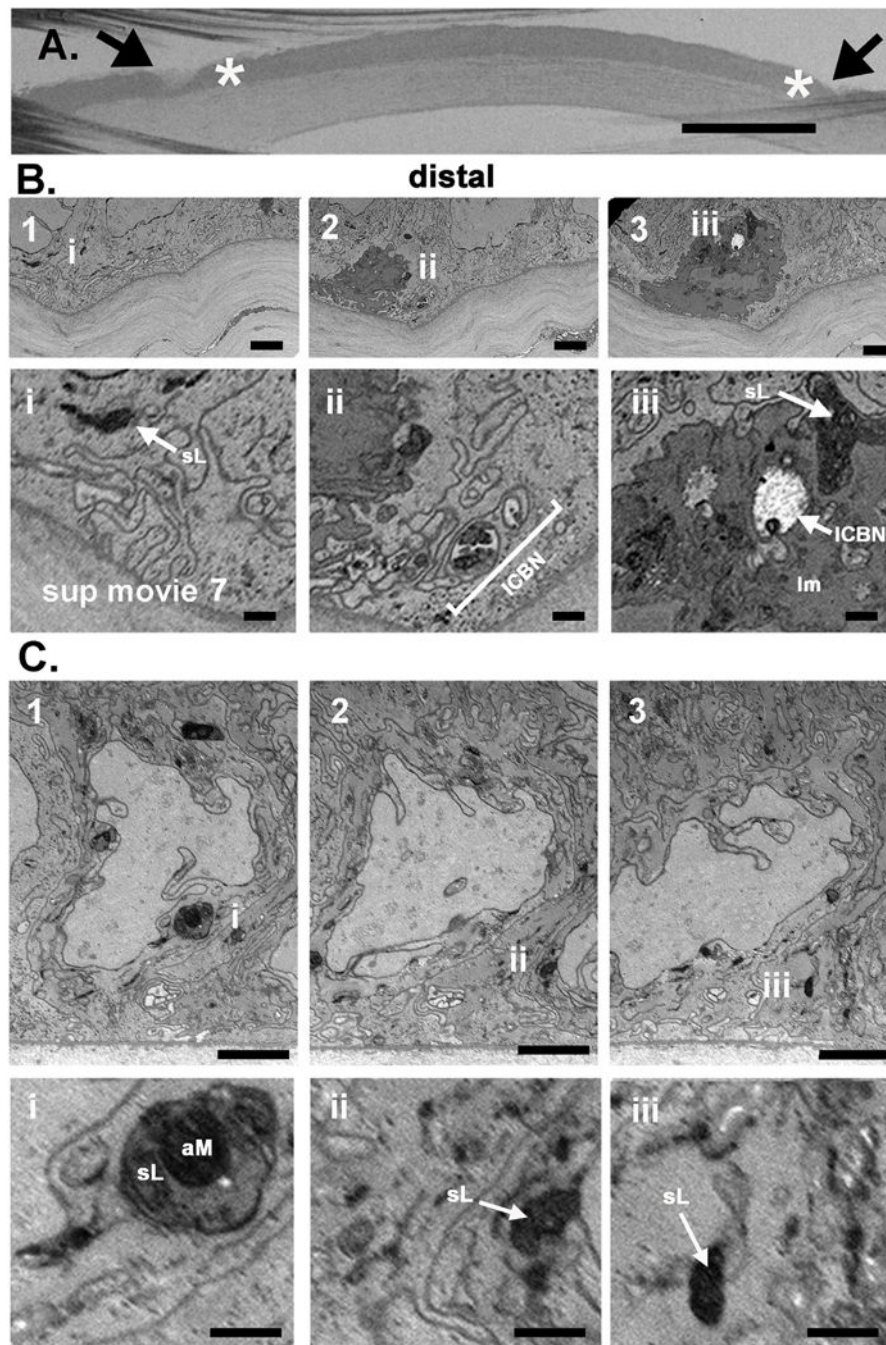


Fig. 7. Corneal epithelial basal cells distal to the injury site contain numerous electron dense organelles of varying sizes consistent with their identification as lysosomes 3 h after trephine injury.

A. A trephine wounded mouse cornea is shown embedded and mounted on the block face. Arrows show sites where the trephine blade crushed or severed axons and asterisks indicate the sites where milling was performed. Bar in A = 400 μ m. **B and C.** Serial images obtained distal to the injury site from two trephine wounded corneas at the epithelial-stromal interface are shown in B1–3 and C1–3. Higher magnification images are shown in B*i-iii* and in C*i-iii*. In B2 and B3 an immune cell is seen. In B*ii* to the right of the

immune cells, an ICN containing several electron dense mitochondria is seen. Epithelial (B1/*Bi* and C1–C3/*Ci-Cii*) and immune cells (B2,B3/*Bii,Biii*) have lysosomes containing electron dense debris. Bars in B and C are 2 μm and bars in *Bi-iii* and *Ci-iii* are 500 nm. Supplemental Movie 7 shows serial sections through the trephine wounded cornea that the images shown in B were obtained from. ICN = intraepithelial corneal basal nerve, sL = secondary lysosome, aM = axonal mitochondria, Im= immune cell.

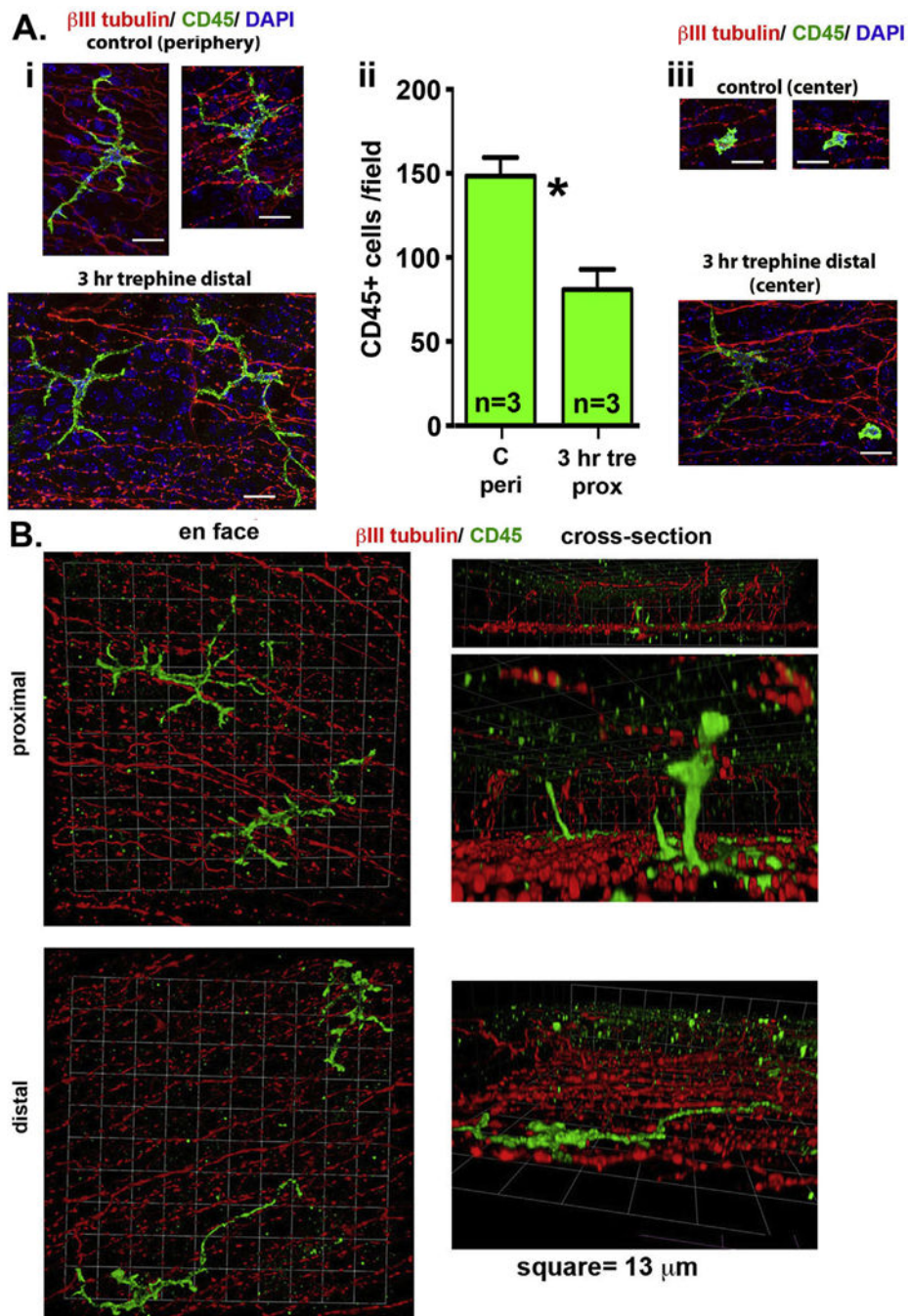
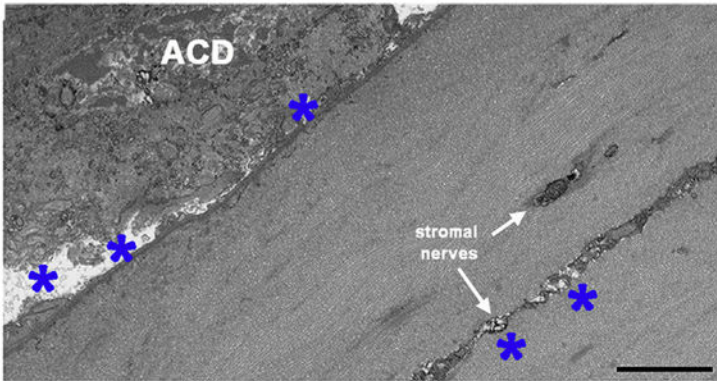
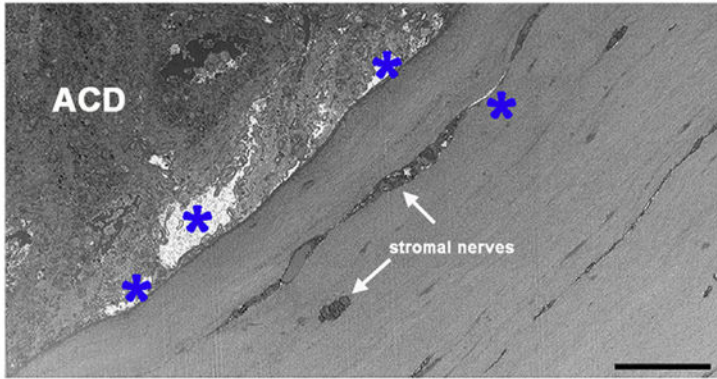


Fig. 8. High resolution confocal imaging of control and trephine wounded corneas at proximal and distal sites show elongated CD45⁺ dendritic cells in the epithelial basal cell layer.

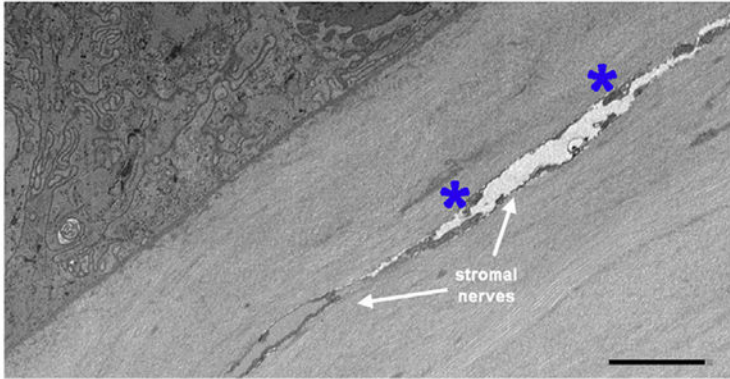
A. 2D projected confocal images 30 μ m thick of whole flat mounted control and trephine wounded corneas 3 h after injury (*i* and *iii*) imaged at distal sites and at the corneal center are presented. Corneas were stained with antibodies against CD45 (green) to show immune cells, β III tubulin (red) to show ICNs, and DAPI to show cell nuclei. Images are projected from below the basement membrane towards the apical aspect of the cornea. CD45⁺ cells with morphologies consistent with dendritic cells are observed. The numbers of CD45⁺ cells

per field were assessed in corneal periphery of control corneas and at proximal sites 3 h after trephine injury (*ii*). There are significantly fewer immune cells per field after injury compared to controls by Student's *t*-test. Bar *Ai* and *Aiii* = 13 μ m. **B.** 3D confocal images are presented of whole flat mounted trephine wounded corneas imaged at proximal and distal sites stained with antibodies against CD45 (green) to show immune cells and β III tubulin (red) to show ICNs. Images are presented *en face* and rotated to generate cross sections. (For interpretation of the references to color in this figure legend, the reader is referred to the Web version of this article.)

A. 3 hr after injury at injury site



3 hr after trephine injury



proximal

B. β III tubulin+ stromal nerves

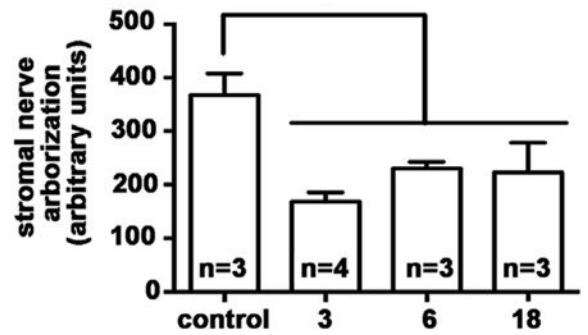
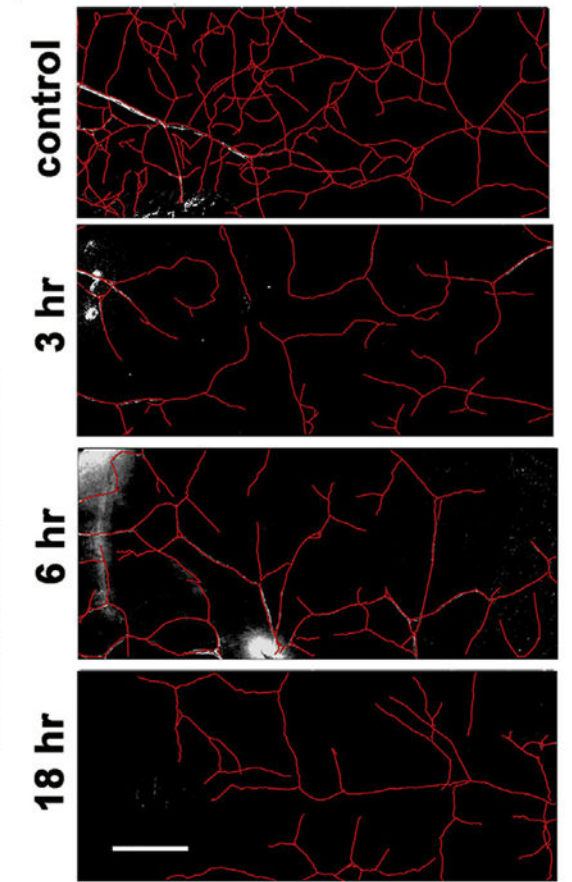


Fig. 9. Stromal cells and nerves are disrupted 3 h after trephine injury.

A. Block face images were obtained 3 h after wounding at two injury sites where the trephine crushed the epithelium and from a region proximal to the trephine injury site. Note that the epithelial cells at the injury sites have been killed by accidental cell death (ACD) with open spaces having formed within the basal aspect of the basal cells above the EBM as axons degenerated (asterisks). While the EBM is not disrupted, clear spaces have formed around some of the stromal cells and stromal nerves (asterisks) indicating that they have been impacted by trephine injury. The image proximal to the trephine injury site shows

healthy epithelial cells and yet the Schwann cell shown is dysmorphic. ACD = accidental cell death. **B.** Stromal nerve arborization was quantified using Neuron J in control, 3, 6, and 18 h after trephine injury. Data show that as early as 3 h, stromal nerve arborization is reduced compared to controls. Asterisks indicate swollen sites around stroma nerves. Bar in B =250 μm .

Author Manuscript

Author Manuscript

Author Manuscript

Author Manuscript